Chemical Engineering Science 280 (2023) 119010

Contents lists available at ScienceDirect

Chemical Engineering Science

journal homepage: www.elsevier.com/locate/ces

Coupled transport and poromechanics model to understand quality evolution during sequential drying

Mayuri S. Ukidwe [a], Ashim K. Datta [a,*], Chris Koh [b], Stacie Tibos [c], John Bows [c]

[a] Department of Biological and Environmental Engineering, Cornell University, Ithaca, NY, USA
[b] PepsiCo. Research and Development, Plano, USA
[c] PepsiCo. Research and Development, Leicester, UK

ARTICLE INFO

Keywords:
Sequential drying
Multi-physics modeling
Poromechanics
Quality evolution

ABSTRACT

Sequential drying provides opportunities to achieve quality by combining individual drying modes. Many process and product parameters affecting multiple drying modes make it complex. We studied quality evolution in a sequence of microwave, impingement, and hot air drying of the mashed vegetable chip using a poromechanics and transport model with volumetric evaporation, moisture-based microwave absorption, pressure-driven expansion, moisture loss-driven shrinkage and glass transition. It was validated for temperature, moisture, size and porosity obtained in an industrial setting. Gas porosity is higher at the center during microwave and at the surface during impingement drying. Moisture loss-driven shrinkage was more dominant than pressure-driven expansion. Shrinkage followed the moisture loss when the chip was rubbery, but shrinkage reduced after the glass transition occurred. Sequential drying was able to achieve a quality that would be hard to achieve using a single drying method. The mechanistic framework, successful for three drying modes and their sequence, is useful to understand drying-like processes.

1. Introduction

There are many drying methods and their final effects on quality are quite different. Hot air convective drying is the most commonly used drying method. However, it removes water from the outer parts of the food more effectively than the internal parts and creates non-uniform moisture distribution. It progressively hinders the advancement of the drying front into the food as resistance to moisture removal increases with drying. Continued drying might impart undesired color, texture and loss of nutritional value due to various chemical reactions and physical changes taking place in the food. Impingement drying is a fast and efficient drying method for thin materials. It heats the materials effectively with high velocity and high air temperature by reducing the thermal boundary layer (Moreira, 2001). Higher drying rates of impingement change the internal structure to the greatest extent (Nowak and Lewicki, 2005) and generate a crispy texture due to faster surface heating (Geedipalli et al., 2008). Microwave drying has also been used as it is more energy efficient (Qing-Guo et al., 2006; Zhang et al., 2017). It can also introduce expansion in the food (Witrowa-Rajchert and Rzaca, 2009; Kowalski et al., 2010). This helps create a structure similar to crispy and fried foods yet results in low-fat content making the foods healthier (Moraru and Kokini, 2003; Gulati et al., 2016; Pompe et al., 2020). It may also result in extremely high temperatures at the corners (Cohen and Yang, 1995), burning (Nijhuis et al., 1998) and undesired color and/or flavor (Khraisheh et al., 2004).

Reliance on a single drying method has been challenging to meet the desired nutrient and flavor retention, browning, uniformity of drying and texture of dried foods (Zhang et al., 2017). Recently, emerging combinations (two or more drying methods used simultaneously) and sequential drying methods have been more useful as they are energy efficient and provide reduced quality degradation (Hnin et al., 2018). Although the simultaneous application of conventional hot air drying with microwave, infrared, ultraviolet, radio frequency, vacuum, freeze or pulsed electric drying is shown to be effective in maintaining product quality and reducing operational costs, the capital cost of the specialized equipment and problems in the scale-up necessary for industrial usage hinder the commercialization of such drying methods (Supmoon and Noomhorm, 2013; Onwude et al., 2019; Zhou and Wang, 2019; Zhang et al., 2017; Hnin et al., 2018; Yin et al., 2019).

* Corresponding author at: 208 Riley-Robb Hall, Ithaca, NY 14853, USA.
E-mail address: akd1@cornell.edu (A.K. Datta).

https://doi.org/10.1016/j.ces.2023.119010
Received 3 March 2023; Received in revised form 30 April 2023; Accepted 14 June 2023
Available online 3 July 2023

Nomenclature

a_w	Water activity	
c_i	Concentration of species i	kg/m^3
$C_{p,i}$	Specific heat capacity of species i	J/(kg · K)
C	Molar density	kmol/m^3
$\mathbf{C}$	Right Cauchy-Green deformation tensor	
$\mathbf{D}$	Stiffness tensor	Pa
D_b	Binary diffusivity of vapor and air mixture	m^2/s
$D_{w,c}$	Capillary diffusivity	m^2/s
E	Elastic modulus	N/m^2
$\mathbf{E}$	Green-Lagrange strain tensor	
$\mathbf{F}$	Deformation gradient tensor	
G	Shear modulus	Pa
h_t	Heat transfer coefficient	W/(m^2 · K)
h_m	Mass transfer coefficient	m/s
$\dot{I}$	Rate of evaporation	kg/(m^3 · s)
$\mathbf{I}$	Identity tensor	
J	Jacobian	
K	Bulk modulus	Pa
k_i	Thermal conductivity of species i	W/(m · K)
$k_{in,i}$	Intrinsic permeability of species i	m^2
$k_{r,i}$	Relative permeability of species i	
K_{evp}	Eaporation rate constant	1/s
Le	Lewis number	
m	Overall mass fraction	
M	Moisture content (dry basis)	kg water/kg dry solid
M_i	Molecular weight of species i	kg/gmol
$\hat{n}$	Unit normal	
$\vec{n}_i$	Flux of species i	kg/(m^2 · s)
Nu	Nusselt number	
p	Pressure	Pa
p_c	Capillary pressure of water	Pa
Pr	Prandtl number	
$\vec{q}$	Heat flux	W/m^2
Q	Microwave source term	W/m^3
r	Radius	m
R	Universal gas constant	J/(mol · K)
Re	Reynolds number	
S_i	Saturation of a fluid phase i	
$\mathbf{S}$	Second Piola-Kirchhoff stress tensor	Pa
t	Time	s
T	Temperature	°C
$\bar{u}$	Displacement	m
$\bar{v}$	Velocity	m/s
x_i	Mole fraction of species i in gas phase	
V	Volume	m^3
W	Strain energy density	J/m^3
$\bar{x}$	Coordinates in spatial frame	m
$\bar{X}$	Coordinates in material frame	m

Greek symbols

β	Coefficient of shrinkage	m^3/kg
ϵ	Strain	
ρ	Density	kg/m^3
λ	Latent heat of vaporization	J/kg
ω	Mass fraction in the gas phase	
Φ	Porosity in Lagrangian frame	
ϕ	Porosity in Eulerian frame	
μ	Shear modulus	Pa
μ_i	Dynamic viscosity of phase i	Pa · s
ν	Poisson's ratio	
$\bar{\sigma}$	Stress	Pa
χ	Transformation of reference frames	

Subscripts and superscripts

0	At time $t = 0$
a	Air
amb	Ambient
b	Binary
c	Capillary
eff	Effective
el	Elastic
eq	Equilibrium
evp	Evaporation
f	Fluid
G	Ground (stationary observer)
g	Gas
i	i^{th} Phase
in	Intrinsic property
M	Moisture
m	Mechanical
$oven$	At ambient conditions of the oven
r	Relative property, r-coordinate
s	Solid
sat	Saturation
$surf$	Surface
$symm$	Symmetry
$\mathbf{T}$	Transpose of a tensor
t	Thermal
v	Water vapor
w	Water
$\bar{\mathbf{x}}$	Coordinate in spatial frame
$\bar{\mathbf{X}}$	Coordinate in material frame
z	z-coordinate

Sequential drying, on the other hand, uses commercially available dryers in sequence to effectively drive the moisture out of foods. Therefore, sequential drying is more suitable for commercial applications. In this study, the sequence of microwave drying, followed by impingement drying, and lastly hot air drying is considered (Fig. 1). The inclusion of microwave drying as a part of the drying sequence is very important and the use of microwave drying as the first stage has been suggested by Kostaropoulos and Saravacos (1995), and Örkan-Karabacak et al. (2020). In the first stage, microwave energy is used to evaporate the water. This controls temperature from reaching a very high value and burning the food. The physics of sequential drying includes quantification of heat and mass transport, fluid flow, evaporation and deformation of a porous material, including simultaneous pressure-driven expansion and moisture loss-driven shrinkage. Additionally, the material properties undergo a large change due to the glass transition. There are multiple variables in each drying stage that affect the quality. Therefore, it is important to study the underlying mechanism affecting each drying stage.

1.1. Previous attempts of modeling the quality evolution

Prior studies of combination drying mainly have been focused on the experimental observation of quality and energy consumption. There have been attempts to calculate the material properties required for Fick's law-based diffusion and Newton's law-based cooling (Eştürk, 2010; Zhao et al., 2014; Argyropoulos et al., 2011). Such regression analysis-based attempts may be simple to use but they have limited applicability. Other attempts of modeling microwave-assisted convective drying include single phase diffusion, convection of water (Yang and

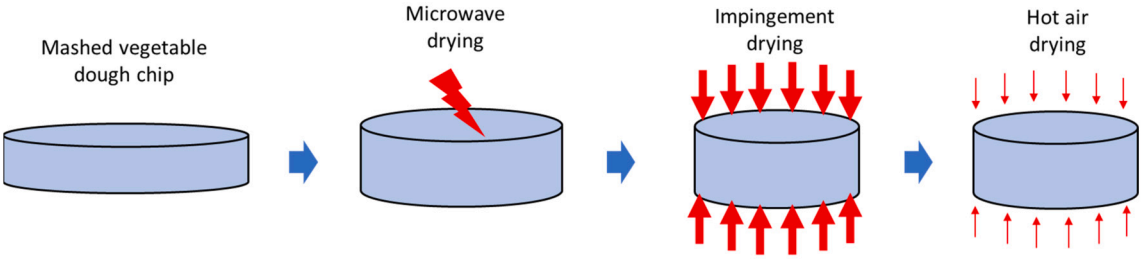

Fig. 1. The sequential drying process for a mashed vegetable chip.

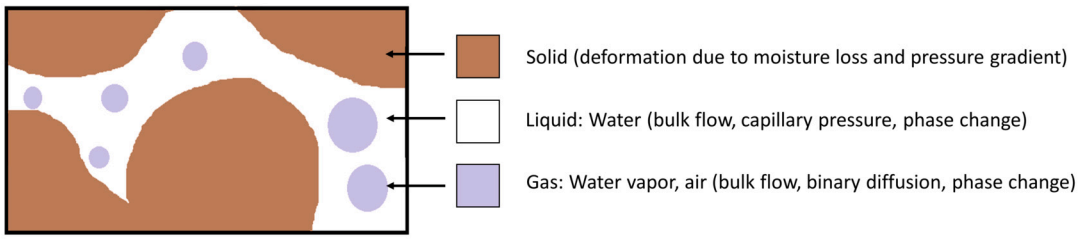

Fig. 2. Representative elementary volume showing multiple phases and underlying physics affecting them during sequential drying.

Gunasekaran, 2001) with the conductive heat transfer, either constant (Workneh and Oke, 2013; Darvishi et al., 2013) or Lambert's law-based (Souraki and Mowla, 2008; McMinn et al., 2003; Kumar et al., 2015) microwave power absorption and vapor-liquid equilibrium.

Although these models include the flow of water in the food, they lack the fundamental understanding of pressure-driven flow in porous media such as food. Malafronte et al. (2012) studied the vapor diffusion, convective transport and evaporation of water without the effect of water activity. In addition to the above-mentioned physics, multi-phase porous media-based approaches, including a distributed microwave power absorption and water activity-dependent non-equilibrium evaporation approach have been combined with expansion (Rakesh and Datta, 2012; Ressing et al., 2007; Kumar and Karim, 2019) and shrinkage (Sanga et al., 2002). More comprehensive studies have included a complex three-dimensional analysis of microwave power absorption using Maxwell equations with (Gulati et al., 2016) and without (Malafronte et al., 2012; Rakesh et al., 2012) the detailed mechanisms of deformation and change in the properties that affect deformation.

1.2. Novelty of the work

We developed a first principle-based mechanistic framework to predict the evolution of quality parameters for a novel mashed vegetable chip dried sequentially using the microwave, impingement and hot air drying. Effects of various product and process parameters were studied for the chip quality as characterized by bulk density, gas porosity, size change and shear modulus. We validated the multiphase, multicomponent transport and poromechanics model that included simultaneous pressure gradient-driven expansion and moisture loss-driven shrinkage, and material transformation using temperature, moisture, size and porosity data from an industrial setting. We extracted the contributions of individual drying methods, their synergistic effect, and the contribution of material transition toward quality development in sequential drying.

1.3. Objectives and overview

Our objectives are (1) to develop a mechanistic framework for the prediction of quality (bulk density, gas porosity and size change) in a sequential drying process where volume expansion and shrinkage both occur simultaneously, (2) to validate the model for an industrial scale process and, (3) to develop insight into the combination of each drying method and the sequence into the quality development. The manuscript is organized as follows: Section 2 describes the multi-component and multi-phase transport and large deformation model formulation, including the pressure gradient and moisture loss-driven deformation and the effect of glass transition; Section 3 includes the experimental procedures and model implementation details; and Section 4 reports the model validation and insights used to understand the effect of each drying step in the sequence on the quality evolution.

2. Model development

2.1. Qualitative description of the modeling process

This section mechanistically describes the sequential drying of a mashed vegetable chip. Assumptions in the mechanistic description, the multi-phase and multi-component transport as well as the deformation of the chip, along with boundary and initial conditions, are also described. The chip, treated as a porous material (Fig. 2), undergoes microwave drying, followed by impingement drying, followed by hot air drying. The distribution of temperature and moisture during drying changes the dielectric, thermophysical and mechanical properties of the chip, which affect the microwave power absorption, transport processes and deformation. The physics of drying, in turn, affect the moisture and temperature distribution. Therefore, this is a two-way coupled problem (Fig. 3).

Microwave drying: The absorption of microwave radiation energy by the chip causes its temperature to rise. This results in internal volumetric evaporation of water. The vapor generated from evaporation inside the chip develops gas pressure. The gas pressure drives the water and gas toward the outer surface of the chip. When the surface gets saturated, water is expelled from the surface as drip loss. Simultaneously, moisture is also lost from the surface of the chip due to hot and dry air flowing over it. Both the internal pressure generation leading to expansion and the moisture loss leading to shrinkage result in the deformation of the chip. This changes the porosity of the material, which in turn affects the transport of water and gases, evaporation and heat transfer in the chip.

Impingement and hot air drying: During convective drying, hot, dry air flows over the chip (at a very high velocity in the case of impingement drying). This causes a higher temperature at the chip surface than inside. When the internal temperature increases, the water evaporates and develops internal pressure. The pressure drives the flow of water and gas similar to microwave drying. Simultaneously, the moisture is lost at the boundary. However, there is no drip loss of water as

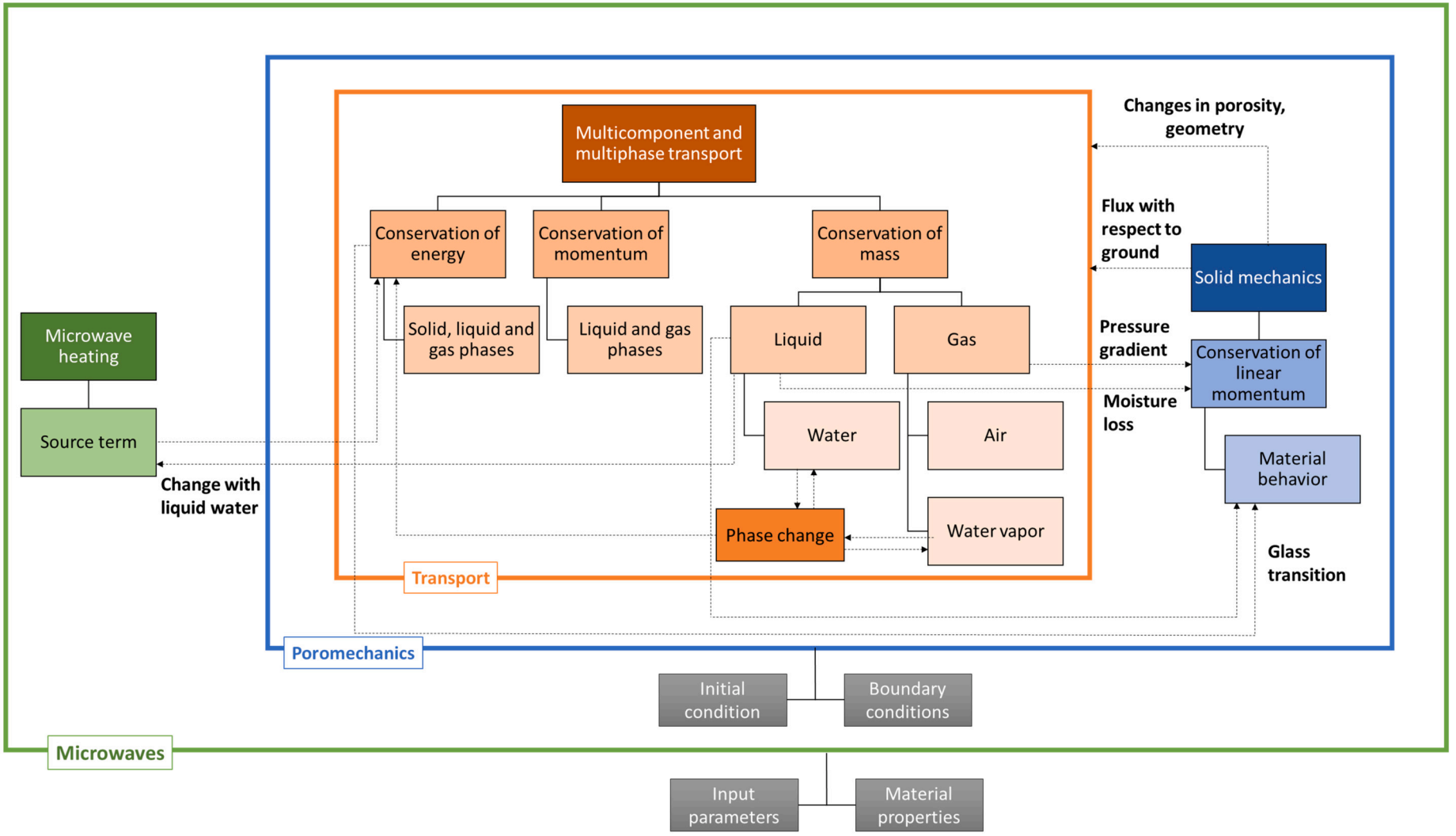

Fig. 3. Flowchart showing the physics formulation and the coupling between multi-phase and multi-physics transport and the deformation during drying.

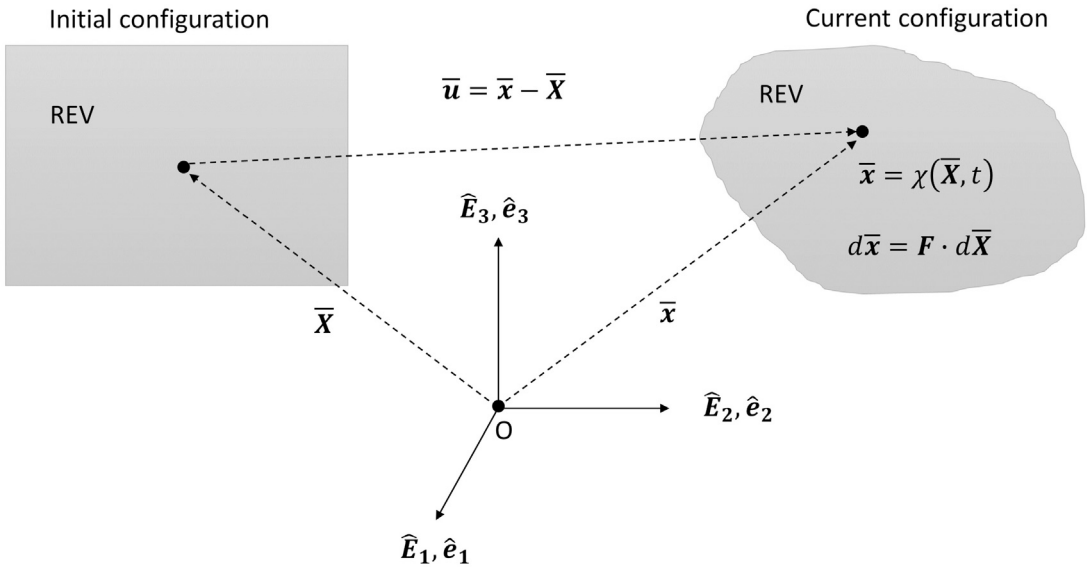

Fig. 4. The initial (reference) and current (deformed) configuration of the representative elementary volume during sequential drying.

the chip surface remains unsaturated. The chip undergoes glass transition and becomes hard and rigid due to a large change in the mechanical properties from the moisture loss and temperature increase. The chip deformation is affected by moisture loss, gas pressure gradient and the glass transition.

Assumptions: The following assumptions were made while formulating the model. (1) The water in the chip pores is at equilibrium with the vapor phase initially. (2) The local thermal equilibrium is assumed at all times. (3) The effects of gravity are neglected. (4) The effect of temperature on the diffusivity of water is neglected. (5) The material is assumed to be nearly incompressible.

2.2. Continuum description

The chip is assumed to be a multi-phase porous medium consisting of solid, liquid (water) and gas (water vapor and air) (Fig. 2). It deforms due to pressure generated by water evaporation and moisture loss. The deformation formulation is based on the poromechanics approach described by Dhall and Datta (2011) and Datta et al. (2012). The total volume of the material is split into solid and fluid phases and is mathematically written as follows.

$$\Delta V = \Delta V_s + \Delta V_f \tag{1}$$

where subscripts s and f denote solid and fluid phases, respectively, and V is the volume of the porous material confined to a representative element. Hereafter, all quantities are written for the representative elementary volume (REV) and homogenized over the entire porous material. The fluid phase consists of water (denoted by w) and gases (denoted by g). The pore volume is assumed to be occupied by the fluid. Hence, the porosity, ϕ, is defined as

$$\phi = \frac{\Delta V_w + \Delta V_g}{\Delta V} \tag{2}$$

Saturation, S_i, of the fluid phase, i, is defined as the ratio of the volume of phase, i, to the pore volume. Therefore,

$$S_i = \frac{\Delta V_i}{\Delta V_f} = \frac{\Delta V_i}{\phi \Delta V} \qquad i = w,\ g \tag{3}$$

where w represents the water phase and g represents the gas phase.

The chip deforms during the sequential drying process. Assuming the mass of the solid is conserved, porosity (ϕ) at a time (t) can be calculated as followed.

$$\rho_s V(t)(1 - \phi(t)) = \rho_s V_0 (1 - \phi_0) \tag{4}$$

$$\phi(t) = 1 - \frac{(1 - \phi_0)}{V(t)/V_0} = 1 - \frac{1 - \phi_0}{J(t)} \tag{5}$$

where $J(t)$ is the ratio of the current volume to the initial volume of the chip and is called the Jacobian. Further discussion about obtaining the Jacobian can be found in Section 2.3.

2.3. Solid mechanics

Deformation during drying of the chip is caused by the internal evaporation of water that results in the pressure gradient and the moisture loss. The Jacobian ($J(t)$) is obtained as the determinant of the deformation gradient tensor, $\mathbf{F}$, which maps the displacement by comparing the geometry of the chip in the deformed (current or the spatial frame) to the undeformed (reference or the material frame). In the Lagrangian description of the motion, the spatial frame coordinates $\overline{\mathbf{x}}$ are described as a function of the material frame coordinates $\overline{\mathbf{X}}$ and time (t) with transformation, χ, (Fig. 4) as follows.

$$\overline{\mathbf{x}} = \chi\left(\overline{\mathbf{X}}, t\right) \tag{6}$$

The displacement of a point $\overline{\mathbf{X}}$ in the material frame to the point $\overline{\mathbf{x}}$ in the spatial frame is denoted by $\overline{\mathbf{u}}$ and is defined as:

$$\overline{\mathbf{u}} = \overline{\mathbf{x}} - \overline{\mathbf{X}} = \chi\left(\overline{\mathbf{X}}, t\right) - \overline{\mathbf{X}} \tag{7}$$

Therefore, the deformation gradient ($\mathbf{F}$) and the Jacobian ($J(t)$) can be obtained from the coordinates as follows:

$$\mathbf{F} = \nabla_X \overline{\mathbf{x}} = \nabla_X \left(\chi(\overline{\mathbf{X}}, t)\right) \tag{8}$$

$$J(t) = \det(\mathbf{F}) \tag{9}$$

2.3.1. Deformation gradient tensor split

In the deformation analysis, the deformation gradient ($\mathbf{F}$) can be used to separate the volume change caused by moisture loss from the volume change that is caused by mechanical effects by splitting $\mathbf{F}$. For small deformation, the split can be additive, whereas, for large deformation, the multiplicative split should be used (Dhall and Datta, 2011; Écsi et al., 2017; Vujošević and Lubarda, 2002). During microwave and convective drying, the chip deforms more than 10%. Therefore, it will be necessary to consider a large deformation and, hence, the multiplicative split of the deformation gradient tensor. During the large deformation, the material is assumed to first undergo stress-free deformation from

moisture loss, and then the mechanical stresses deform the material further. This is represented mathematically, using the deformation gradient from moisture loss ($\mathbf{F_M}$), and that due to the mechanical stresses ($\mathbf{F_{el}}$).

$$\mathbf{F} = \mathbf{F_{el}} \cdot \mathbf{F_M} \tag{10}$$

2.3.2. Conservation of linear momentum

Using Tarzaghi's effective stress principle, we can write the stress on the REV, $\bar{\sigma}$, as a total of the stress on the solid skeleton, $\overline{\sigma}'$, and the fluid pressure (p_f) in pores (Dhall and Datta, 2011).

$$\overline{\sigma} = \overline{\sigma}' - p_f \mathbf{I} \tag{11}$$

The fluid pressure (p_f) can be expressed as volume averaged pressure exerted by liquid and gas phases as follows:

$$p_f = S_w p_w + S_g p_g \tag{12}$$

Assuming the quasi-steady state deformation, the solid momentum balance results in a zero divergence state.

$$\nabla \cdot \overline{\sigma} = 0 \tag{13}$$

Hence, from Eqs. (11) and (13), the divergence of the stress on the solid can be written as

$$\nabla_X \cdot \overline{\sigma}' = \nabla_X p_f = \nabla_X (S_w p_w + S_g p_g) = 0 \tag{14}$$

The pressure of the water is considered to be the result of pressure from the opposing action of the gas pressure and the capillary action (Datta et al., 2012).

$$p_w = p_g - p_c \tag{15}$$

From Eqs. (14) and (15), we can write,

$$\nabla_X \cdot (\overline{\sigma}' + S_w p_c \mathbf{I}) = \nabla_X p_g \tag{16}$$

With the effect of moisture loss accounted for as the deformation gradient $\mathbf{F_M}$, the linear momentum balance equation can be re-written in terms of the stress from the mechanical load only, $\overline{\sigma}''$, i.e., the effective stress on the solid skeleton, $\overline{\sigma}'$, plus the volume averaged capillary pressure, p_c.

$$\nabla_X \cdot (\overline{\sigma}' + S_w p_c \mathbf{I}) = \nabla_X \cdot \overline{\sigma}'' = \nabla p_g \tag{17}$$

The effective stress on the solid skeleton $\overline{\sigma}''$ is defined in the Lagrangian coordinate system in terms of the second Piola–Kirchhoff stress, $\mathbf{S}$, and the deformation gradient tensor ($\mathbf{F}$) due to mechanical strain.

$$\overline{\sigma}'' = J^{-1} \mathbf{F} \cdot \mathbf{S} \cdot \mathbf{F^T} \tag{18}$$

The second Piola-Kirchhoff stress tensor $\mathbf{S}$ characterizes the material behavior and is related to the strain energy density function, W_s. It can be derived using the Green-Lagrange tensor for elastic strains, $\mathbf{E_{el}}$, with the second law of thermodynamics.

$$\mathbf{S} = \frac{\partial W_s}{\partial \mathbf{E_{el}}} \tag{19}$$

The strain energy density function, W_s, depends on the chosen material model. The details about the strain energy density function are described in Section 2.3.3. The Green-Lagrange elastic strain tensor, $\mathbf{E_{el}}$, is given by

$$\mathbf{E_{el}} = \frac{1}{2}(\mathbf{F_{el}^T F_{el}} - \mathbf{I}) \tag{20}$$

2.3.3. Constitutive law

The constitutive behavior of the material is characterized by the strain energy density function W_s as mentioned in Section 2.3.2. It is important to assess the effect of glass transition, the contribution of viscous effects and the Deborah number (calculated as the ratio of stress relaxation time and the processing time) to understand the appropriate material model (Singh et al., 2004; Gulati and Datta, 2015). In the rubbery state, the primary rotational oscillatory tests suggest the relaxation time of the order of 10^{-3} to 10^{-4} s. With the processing time being of the order of 10^{1} to 10^{2} s, the low Deborah number (10^{-4} to 10^{-6}) suggests that the viscous contributions are important. In the glassy state, the relaxation time is very large suggesting the time-independent viscous contribution. Hence, the elastic material behavior will be applicable. The contribution of the viscous terms could also be significant in the glass transition zone (Singh et al., 2004). Due to a very thin cross-section of the chip, the moisture and temperature distributions exhibit sharp changes at the edges. This maintains most of the chip in the glassy or rubbery region, leaving very little room for the transition zone. Secondly, because of the lack of precise information regarding the size of the transition zone in the literature, it is not possible to incorporate viscous contributions in the transition zone. Thirdly, the force-deformation curves for the steam-cooked sweet potato (Gallego-Castillo and Ayala-Aponte, 2018; Truong et al., 1998) and the stress-strain curves for mashed potato (Krokida and Maroulis, 2000; Gulati and Datta, 2015), two major components of the chip, suggest non-linear elastic or hyperelastic behavior (Belytschko et al., 2013; Dhall and Datta, 2011; Gulati et al., 2016; Krokida et al., 1999; Rakesh and Datta, 2011, 2012). Preliminary simulation of the process with a linear elastic, linear viscoelastic and a neo-Hookean material model showed little difference (see Section 4.4 for details) in the model predictions. Hence, the linear elastic material model Eq. (21) was chosen to avoid further computational complexity.

$$W_s = \frac{1}{2}\mathbf{E_{el}} : \mathbf{C} : \mathbf{E_{el}} \tag{21}$$

where $\mathbf{C}$ is the right Cauchy-Green deformation tensor ($= \mathbf{F^T} \cdot \mathbf{F}$)

2.3.4. Volume change from moisture loss

Under stress-free conditions (Fig. 5), the change in the volume of the REV is due to the changes in the moisture content. The moisture content changes because of the loss of liquid water and vapor at the boundary. Since the density of water is three orders of magnitude higher than that of vapor, the volume change due to the loss of vapor is negligible compared to the loss of liquid water. Therefore, for a REV, the change in volume because of moisture loss can be calculated based on the initial volume, V_0, and the current volume, V_M, as:

$$V_M - V_0 = \frac{c_w V(t) - c_{w,0} V_0}{\rho_w} \tag{22}$$

$$\frac{V_M}{V_0} = J_M = \frac{1 - \phi_0 S_{w,0}}{1 - \phi S_w} \tag{23}$$

The deformation gradient from moisture loss, $\mathbf{F_M}$, is expressed in terms of the water concentration difference and an isotropic coefficient, β, that represents the change in volume with a unit change in concentration of water.

$$\mathbf{F_M} = J_M \mathbf{I} = \mathbf{I} + \beta \left(c_w - c_0'\right) \mathbf{I} \tag{24}$$

From Eq. (24), it can be seen that the coefficient $\beta = 1/\rho_w$ and c_0' refers to the concentration at the stress-free (initial) conditions.

2.3.5. Structural velocity

The description of multiphase and multicomponent transport differs for the deforming solid and a stationary observer at the ground. To calculate the effect of the deforming solid for an observer stationary on the ground, we need to consider the additional velocity arising from solid deformation as follows:

$$\vec{v}_s = \frac{d\overline{\mathbf{u}}}{dt} \tag{25}$$

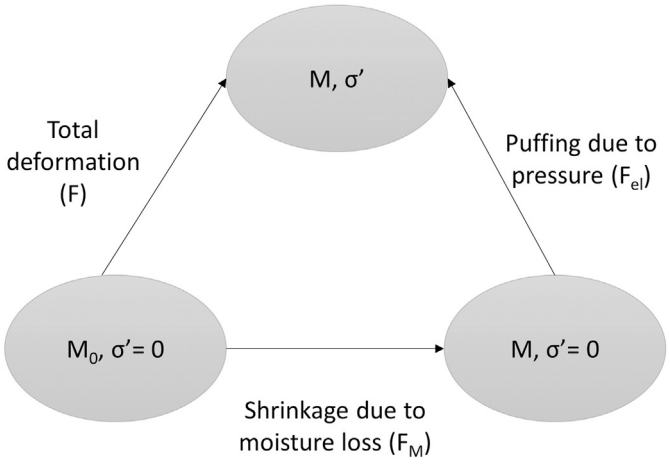

Fig. 5. Multiplicative split of the deformation tensor showing independent deformation due to moisture loss and the mechanical effects contribute to the total deformation.

2.4. Multi-phase and multi-component transport (momentum, mass, and energy conservation)

The multiphase and multicomponent transport in this section has been formulated with respect to an observer stationary at the ground as described in the following expression:

$$\underbrace{\vec{n}_{i,G}}_{\text{Flux relative to ground frame}} = \underbrace{\vec{n}_{i,s}}_{\text{Flux relative to deforming solid}} + \underbrace{c_i \vec{v}_s}_{\text{Additional flux due to solid movement}} \tag{26}$$

where c_i is the concentration of the species 'i' in the porous media.

2.4.1. Momentum conservation

The flow of fluids in porous media is described by Darcy's law. The velocity of the fluid i, in relation to the deforming solid, $\vec{v}_{i,s}$ is given by,

$$\vec{v}_{i,s} = -\frac{k_{in,i} k_{r,i}}{\mu_i} \nabla_X p_i \tag{27}$$

The velocity of water is calculated by considering the water pressure, p_w, which depends on the total gas pressure and the capillary pressure. The velocity of water vapor and the air are similarly calculated as driven by the total gas pressure. It should be noted that when the multi-phase and multi-component transport equations are formulated with respect to the ground, the pressure gradient in the above equation should be calculated in the spatial coordinates.

2.4.2. Mass conservation

The mass conservation equations of water (Eq. (28)), vapor (Eq. (29)), and gas (water vapor + air) (Eq. (30)) with $\dot{I}$ as evaporation rate, as follows.

$$\frac{\partial c_w}{\partial t} + \nabla_x \cdot \vec{n}_{w,G} = -\dot{I} \tag{28}$$

$$\frac{\partial c_v}{\partial t} + \nabla_x \cdot \vec{n}_{v,G} = \dot{I} \tag{29}$$

$$\frac{\partial c_g}{\partial t} + \nabla_x \cdot \vec{n}_{g,G} = \dot{I} \tag{30}$$

2.4.3. Mass fluxes

The mass fluxes, $\vec{n}_{i,G}$, in Eqs. (28), (29) and (30) are calculated based on the fluid pressure, intrinsic permeability, $k_{in,i}$, relative permeability $k_{r,i}$ and viscosity of the fluid μ_i of fluid i. The function $f(\phi)$ accounts for the porosity-based changes in the intrinsic permeability with deformation (see Section 2.5.4 for details).

Liquid water flux: The flux of water in Eq. (28) is calculated by considering the pressure of water in the porous medium that drives the flow. The pressure of water is determined from the gas pressure and the capillary pressure as described by Eq. (15). The flux of water can be calculated as

$$\vec{n}_{w,G} = -\rho_w \frac{k_{in,w} f(\phi) k_{r,w}}{\mu_w} \nabla_x p_w \tag{31}$$

$$\vec{n}_{w,G} = -\rho_w \frac{k_{in,w} f(\phi) k_{r,w}}{\mu_w} \nabla_x (p_g - p_c) \tag{32}$$

$$\vec{n}_{w,G} = -\rho_w \frac{k_{in,w} f(\phi) k_{r,w}}{\mu_w} \nabla_x p_g + \rho_w \frac{k_{in,w} f(\phi) k_{r,w}}{\mu_w} \nabla_x p_c \tag{33}$$

The first term on the right-hand side of the above equation can be simplified as the Darcy velocity of water from Eq. (27). The second term can also be simplified by considering the capillary pressure as a function of moisture content and temperature. Ignoring the dependence of the capillary pressure on the temperature, the gradient of the capillary pressure can be expressed in terms of the gradient of moisture content alone as follows:

$$\vec{n}_{w,G} = \rho_w \vec{v}_{w,G} + \rho_w \frac{k_{in,w} f(\phi) k_{r,w}}{\mu_w} \frac{\partial p_c}{\partial c_w} \nabla_x c_w \tag{34}$$

By defining the capillary diffusivity as

$$D_{w,c} = -\rho_w \frac{k_{in,w} f(\phi) k_{r,w}}{\mu_w} \frac{\partial p_c}{\partial c_w} \tag{35}$$

the flux of water with respect to the ground can be written as

$$\vec{n}_{w,G} = \underbrace{\rho_w \vec{v}_{w,G}}_{\text{Bulk flow of water due to gas pressure}} - \underbrace{D_{w,c} \nabla_x c_w}_{\text{Flux due to capillary diffusion}} \tag{36}$$

Vapor flux: The mass flux of vapor arises from the evaporation of water and diffusion of water vapor and air treated as a concentrated binary mixture (Bird et al., 2007). The mass fraction of water vapor and air is used to calculate the concentration of the respective components.

$$\vec{n}_{v,G} = -\rho_v \frac{k_{in,v} f(\phi) k_{r,v}}{\mu_v} \nabla_x p_g - \phi S_g \left(\frac{C_g^2}{\rho_g} \right) M_v M_a D_b \nabla_x x_v \tag{37}$$

From Eq. (27), we then write the total vapor flux as:

$$\vec{n}_{v,G} = \underbrace{\rho_v \vec{v}_{v,G}}_{\text{Bulk flow of vapor due to gas pressure}} \underbrace{- \phi S_g \left(\frac{C_g^2}{\rho_g} \right) M_v M_a D_b \nabla_x x_v}_{\text{Flux due to binary diffusion}} \tag{38}$$

Total gas flux: The flow of the gas is from the pressure of gas arising from the evaporation of water. We consider the equimolar counter diffusion of water vapor and air. Hence, the effective diffusive flux of total gas is zero. Considering this, the gas flux can be written based on the pressure-driven bulk flow:

$$\vec{n}_{g,G} = -\rho_g \frac{k_{in,g} f(\phi) k_{r,g}}{\mu_g} \nabla_x p_g = \rho_g \vec{v}_{g,G} \tag{39}$$

2.4.4. Energy conservation

The energy equation in the conservative form is written by considering the change in storage, convection due to the bulk flow, conduction of heat, the evaporation-condensation and microwave power absorbed by the chip.

$$\frac{\partial}{\partial t} \left(\sum_{i=s,w,v,a} \rho_i c_{p,i} T \right) + \nabla_x \cdot \left(\sum_{i=w,v,a} \vec{n}_{i,G} c_{p,i} T \right) = \nabla_x \cdot \left(k_{eff} \nabla_x T \right) - \lambda \dot{I} + Q \tag{40}$$

Simplifying the above equation, and using the equation of continuity, the energy equation can be written as follows, which resembles the non-conservative form.

$$\left(\rho c_p\right)_{eff}\frac{\partial T}{\partial t}+\left(\sum_{i=w,v,a}\vec{n}_{i,G}c_{p,i}\right)\cdot\left(\nabla_x T\right)=\nabla_x\cdot\left(k_{eff}\nabla_x T\right)-\lambda\dot{I}+Q \quad (41)$$

The thermophysical properties and the microwave heating term 'Q' in the above equation are described in Section 2.5.

2.4.5. Phase change

Equilibrium and non-equilibrium approaches have been used to model the evaporation rate in the porous media. With microwave and impingement heating generating very high fluxes in a relatively small process time of 50 s to 100 s, we need to assume the non-equilibrium approach to model evaporation. The evaporation/condensation rate is modeled to be volumetrically distributed in the computational domain. Since the method of heating is intense, there is a large amount of moisture removal in a short time. For such processes, it will be more appropriate to use the non-equilibrium evaporation rate (Halder et al., 2007) and can be written as

$$\dot{I}=K_{evp}(S_w)\phi S_g\left[p_v^{sat}(T)a_w(M,T)-p_v\right]\frac{M_v}{RT} \quad (42)$$

The term $p_v^{sat}(T)a_w(M,T)$ is the equilibrium vapor pressure and the difference between the equilibrium vapor density and the vapor density at any location gives the evaporation rate. The evaporation rate constant, K_{evp}, depends on the process to be modeled (Halder et al., 2007). For a fast process, such as microwave or impingement heating, a value of 100 1/s is considered here. Moreover, when the pores are mostly empty (assumed when $S_w \le 0.01$), the residual water is strongly bound to the solid matrix, resulting in high capillary forces. Due to the unavailability of water for evaporation, the evaporation rate is assumed to be zero. Similarly, when the pores are completely saturated (assumed when $S_w \ge 0.99$), there is hardly any space for the liquid to evaporate (very low gas porosity). This restricts the evaporation as well (Bénard et al., 2005). Both conditions are considered in the formulation by assuming the evaporation rate constant to be zero at very high or very low water saturation.

2.5. Input parameters

Refer to Table 1 for the input parameters.

2.5.1. Thermophysical properties

The thermophysical properties in Eq. (41) are weighted averages and estimated as follows:

$$\rho_{eff}=(1-\phi)\rho_s+\phi\left[S_w\rho_w+S_w\left(\omega_v\rho_v+\omega_a\rho_a\right)\right] \quad (43)$$

$$k_{eff}=(1-\phi)k_s+\phi\left[S_w k_w+S_w\left(\omega_v k_v+\omega_a k_a\right)\right) \quad (44)$$

$$c_{p,eff}=m_s c_{p,s}+m_w c_{p,w}+\left(1-m_s-m_w\right)\left(\omega_v c_{p,v}+\omega_a c_{p,a}\right) \quad (45)$$

where m_i is the weight fraction of the phase i.

2.5.2. Transfer coefficients

The heat and the mass transfer coefficients for the microwave drying were assumed based on the work by Rakesh and Datta (2012) and, Ni and Datta (1999). The heat transfer coefficient for the impingement and the hot air drying was calculated based on the correlation for the flow over a flat plate using the oven air temperature and the velocity and accounting for the shrinking diameter, $l(t)$, of the chip Incropera and DeWitt (1990); Warning et al. (2012); Gulati and Datta (2015).

$$Nu=\frac{h_t l(t)}{k_a}=0.0664\frac{Re^{0.5}}{Pr^{0.33}} \quad (46)$$

The mass transfer coefficient in the impinger was calculated based on the modified Chilton-Colburn analogy.

$$h_m=0.5\frac{h_t D_b Le^{0.33}}{k_v}=0.5\frac{h_t D_b}{k_v}\left(\frac{k_v}{\rho_g C_{p,g} D_b}\right)^{0.33} \quad (47)$$

2.5.3. Mechanical properties and glass transition

The chip consists of starch that is made of amorphous and crystalline polymer chains, making the material semi-crystalline. Based on the thermodynamic state of the medium, the polymer chains are arranged in the material. It is theorized that there is free space in the material that is not occupied by the polymer chains (Young and Lovell, 2011). This allows the molecules to change their conformation freely. This translates to a low viscosity and stiffness for the bulk properties. As the temperature of the material increases during drying, the free volume increases allowing easier flow or deformation of the material. Similarly, higher moisture content (acting as a plasticizer) improves the mobility of the polymer chains (Benczedi et al., 1998; Sperling, 2005; Yang et al., 2005), which also decreases the viscosity. As moisture content and temperature decrease, the stiffness of the material increases. This also makes the material brittle or glass-like. This transition is termed the glassy transition and is represented by T_g, the glass transition temperature, and is a function of moisture content. The glass transition curve of potato starch (Benczedi et al., 1998; Gulati and Datta, 2015) is used to simulate the mashed vegetable chip as potato is a major component of the vegetable chip. The mechanical properties (the elastic modulus and Poisson's ratio) are changed when the state of the material changes.

2.5.4. Porosity factor

During the drying process, the chip undergoes large deformation. Depending on the degree of shrinkage or puffing, the porosity increases or decreases. Note that the porosity referred to here (as defined in Eq. (2)) is the total porosity and not the gas porosity that is regularly considered. As the porosity of the material decreases, it becomes less permeable to the flow of the fluids. The Kozney-Carman equation (Bear, 1972) provides a means to account for the changes in the liquid and the gas permeability by multiplying a porosity factor.

$$f(\phi)=\left(\frac{\phi}{\phi_0}\right)^3\left(\frac{1-\phi_0}{1-\phi}\right)^2 \quad (48)$$

2.5.5. Microwave heating

Energy absorbed by the chip during microwave drying depends on the penetration depth of the waves into the chip. As the chip size is very thin, microwave power absorption can be assumed to be initially uniform. The initial microwave power was estimated based on the temperature profile of the sample at the center for the first 10 s. As the concentration of liquid water in the chip reduces, the microwave power absorption also falls below the initial absorption. This reduces the effect of microwave radiation as drying progresses. A similar reduction can be seen when the fully coupled electromagnetism model is used (Ni et al., 1999; Zhang and Datta, 2003; Chen et al., 2015; Gulati et al., 2016). Without a fully coupled microwave model, the reduced absorption of the microwave power needs to be empirically included. Rakesh and Datta (2012) measured the initial power absorption and assumed uniform power distribution in the foods due to small volume, and the microwave power was scaled empirically to account for the moisture loss. The scaling was based on the dielectric properties of leather (Metaxas and Meredith, 1983; Ni, 1997), assuming reasonable similarity in the composition of the raw/blanched potato. A similar approach was followed in determining microwave power absorption. However, the composition of the chip is much different from potato or leather. Therefore, different scaling was required to match the temperature and moisture histories. The initial microwave absorption by the chip was estimated based on the temperature profile of the sample at the center of the chip for the first 10 s, assuming no evaporation, bulk flow and conduction occurred during this time. The empirical power reduction was also obtained by the sensitivity analysis on the exponential factor to fit the measured temperature profile at the center. Therefore, the final form of microwave power was

$$Q=7\times10^7\left(\frac{M_0}{M}\right)^{-3}\ \mathrm{W/m^3} \quad (49)$$

Table 1
Input parameters used in the sequential drying.

Parameter	Value	Unit	Reference
	Dimensions		
Diameter	55	mm	This study
Thickness	2.4	mm	This study
	Density		
Water, ρ_w	998	kg/m^3	(McCabe et al., 2005)
Vapor, ρ_v	Ideal gas	kg/m^3	
Air, ρ_a	Ideal gas	kg/m^3	
Solid, ρ_s	1564	kg/m^3	(Choi and Okos, 1986)
	Specific heat capacity		
Water, c_{pw}	4178	J/kg·K	(McCabe et al., 2005)
Vapor, c_{pv}	2062	J/kg·K	(McCabe et al., 2005)
Air, c_{pa}	1006	J/kg·K	(McCabe et al., 2005)
Solid, c_{ps}	1650	J/kg·K	(Choi and Okos, 1986)
	Thermal conductivity		
Water, k_w	0.57	W/m·K	(McCabe et al., 2005)
Vapor, k_v	0.026	W/m·K	(McCabe et al., 2005)
Air, k_a	0.026	W/m·K	(McCabe et al., 2005)
Solid, k_s	0.21	W/m·K	(Choi and Okos, 1986)
	Intrinsic permeability		
Water, $k_{in,w}$	5×10^{-16}	m^2	(Ni and Datta, 1999)
Gas, $k_{in,g}$	1×10^{-15}	m^2	(Ni and Datta, 1999)
	Relative permeability		
Water, $k_{r,w}$	$[(S_w-0.09)/0.91]^3, S_w > 0.09$ $0, S_w \le 0.09$		(Bear, 1972; Datta et al., 2012)
Gas, $k_{r,g}$	$(1-1.1S_w), S_w < 1/1.1$ $0, S_w \ge 1/1.1$		(Bear, 1972; Datta et al., 2012)
	Viscosity		
Water, μ_w	9.88×10^{-4}	Pa·s	(McCabe et al., 2005)
Gas, μ_g	1.8×10^{-5}	Pa·s	(McCabe et al., 2005)
	Diffusivity		
Water, D_c	$1\times10^{-8}\exp(-2.8+2M)$	m^2/s	(Ni et al., 1999)
Gas, D_b	2.6×10^{-5}	m^2/s	(Rakesh et al., 2012)
	Mechanical properties		
Poisson's ratio, ν	0.49 (rubbery) 0.3 (glassy)		(Gulati and Datta, 2015)
Shear modulus, G	Fig. 6b	Pa	This study
	Other properties		
Heat transfer coefficient, h_t	Fig. 7a	W/m^2·K	This study
Mass transfer coefficient, h_m	Fig. 7b	m/s	This study
Oven temperature, T_{oven}	Fig. 7c	K	This study
Latent heat of vaporization, λ	2.26×10^6	J/kg·K	(McCabe et al., 2005)
Saturation vapor pressure, p_v^{sat}	$\frac{101325}{760}\times10^{8.07131-\frac{1730.63}{T-39.724}}$ $274.15 \le T \le 373.15$ $\frac{101325}{760}\times10^{8.14019-\frac{1810.94}{T-28.665}}$ $272.15 \le T \le 647.15$	Pa	(Warning et al., 2012)
Water activity, a_w	$0.2699 + 0.4479\ln(M)$		This study

2.6. Initial and boundary conditions

2.6.1. Initial conditions

The initial displacement in the sample was assumed to be zero.

$$\bar{\mathbf{u}}_{t=0} = 0 \text{ m} \tag{50}$$

The initial temperature of the chip was assumed to be 20 °C.

$$T_{t=0} = 293.15 \text{ K} \tag{51}$$

The initial concentration of water in the chip was calculated from the recipe.

$$c_{w,t=0} = 685 \text{ kg/m}^3 \tag{52}$$

The initial mass fraction of water vapor in the gas phase was calculated by assuming water and vapor are at equilibrium at the beginning of the process. The initial temperature and the water activity of the mashed dough were used to calculate the concentration of vapor based on the moisture isotherm.

$$\omega_{v,t=0} = 0.0014 \tag{53}$$

The porous medium was assumed to be at atmospheric pressure in the beginning.

$$p_{t=0} = 101325 \text{ Pa} \tag{54}$$

2.6.2. Boundary conditions

The boundaries on the axis of symmetry and the plane of symmetry (Fig. 8), were set to zero flux condition (Eqs. (55) and (56)) for the multicomponent and multiphase transport, and zero normal displacements (Eqs. (57) and (58)). All other boundaries were set to be unconstrained and free to deform.

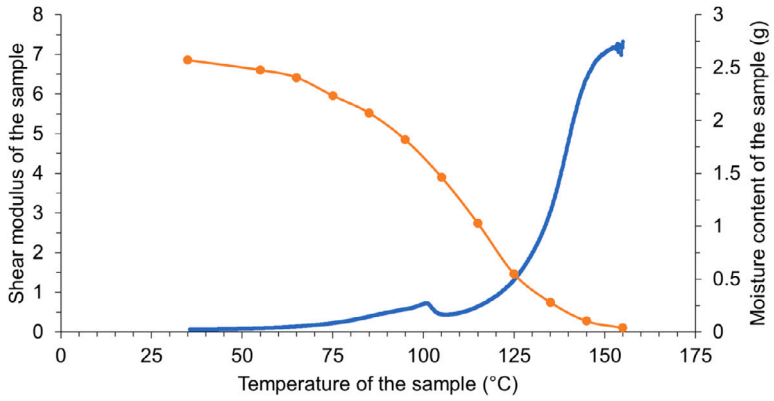

(a)

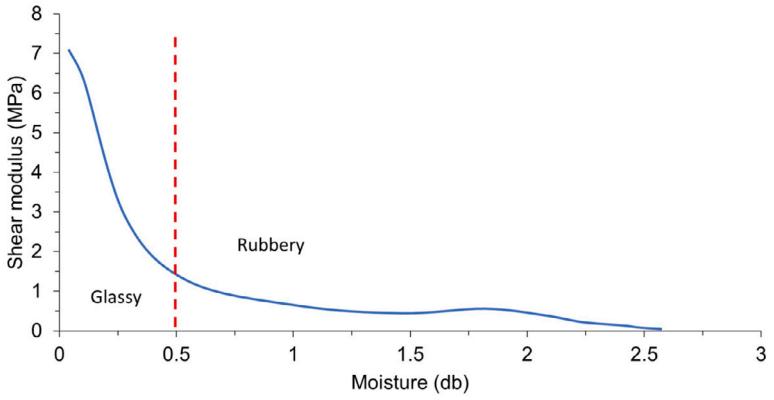

(b)

Fig. 6. (a) Experimentally measured shear modulus and moisture content variation with temperature and (b) Estimated variation in the shear modulus with moisture content change.

$$-\hat{n}\cdot\vec{n}_{i,G|\text{symm}}=0 \quad i=w,\ v,\ a,\ g \tag{55}$$

$$-\hat{n}\cdot\vec{q}_{G|\text{symm}}=0 \tag{56}$$

$$u_r=0 \text{ at } r=0 \tag{57}$$

$$u_z=0 \text{ at } z=0 \tag{58}$$

The pressure was set to ambient conditions for the boundaries exposed to the atmosphere.

$$p_{|surf}=101325 \text{ Pa} \tag{59}$$

The liquid water moves from the interior of the chip to the surface by capillary diffusion and the bulk flow, and evaporates before getting convected away as vapor. Similarly, when the pores at the surface are saturated ($S_w \geq 0.99$), the water can also leave the chip due to drip loss. The movement of the boundary also creates an additional flux. Therefore, the flux of water at the surface, with respect to the ground, can be written as

$$-\hat{n}\cdot\vec{n}_{w,G|\text{surf}}=h_m\phi S_w\left(\rho_v-\rho_{v,\text{oven}}\right)+\underbrace{\rho_w\hat{n}\cdot\vec{v}_{w,G}}_{\text{When } S_w\geq 0.99}+c_w\hat{n}\cdot\vec{\boldsymbol{v}}_s \tag{60}$$

The water vapor in the chip moves to the surface via binary diffusion and bulk flow. At the surface, the vapor is convected away. Due to large pressure gradients near the surface, the vapor also may undergo blowing. Hence, the flux of the vapor, with respect to the ground, can be written as

$$-\hat{n}\cdot\vec{n}_{v,G|\text{surf}}=h_m\phi S_g\left(\rho_v-\rho_{v,\text{oven}}\right)+\underbrace{\rho_v\hat{n}\cdot\vec{v}_{v,G}}_{\text{Blowing flux}}+c_v\hat{n}\cdot\vec{\boldsymbol{v}}_s \tag{61}$$

Similarly, the concentration of air in the chip decreases and causes an influx of air into the chip from the environment. This is included as the convective flux in the equation below. The air influx maintains a certain minimum air concentration in the chip at high vaporization. The air may be blown out of the chip from the high internal pressure as well.

$$-\hat{n}\cdot\vec{n}_{a,G|\text{surf}}=h_m\phi S_g\left(\rho_a-\rho_{a,\text{oven}}\right)+\underbrace{\rho_a\hat{n}\cdot\vec{v}_{a,G}}_{\text{Blowing flux}}+c_a\hat{n}\cdot\vec{\boldsymbol{v}}_s \tag{62}$$

Depending on the temperature of the oven, the chip is subjected to convective cooling or heating (the first term of Eq. (63)). The loss of water occurs in the liquid and gas phases when the water evaporates at the surface. This needs to be specifically accounted for when calculating the heat flux. Some of the water leaving the system evaporates and is then convected away as vapor. Hence, the corresponding contributions of latent heat and sensible heat need to be counted. The water is expelled from the surface due to gas pressure when the surface is saturated. This is included in the third term of Eq. (63). Additionally, there is a loss of sensible heat from the transport of water vapor and air (the fourth and the fifth terms in Eq. (63)), respectively) across the boundary.

$$\begin{aligned}-\hat{n}\cdot\vec{q}_{G|\text{surf}}=&\,h_t\left(T-T_{\text{oven}}\right)-h_m\phi S_w\left(\rho_v-\rho_{v,\text{oven}}\right)\left(\lambda+c_{p,w}T\right)\\&-\underbrace{\left(c_w\hat{n}\cdot\vec{v}_{w,G}\right)c_{p,w}T}_{\text{When } S_w\geq 0.99}-\left(-\hat{n}\cdot\vec{n}_{v,G|\text{surf}}\right)c_{p,v}T-\left(-\hat{n}\cdot\vec{n}_{a,G|\text{surf}}\right)c_{p,a}T\end{aligned} \tag{63}$$

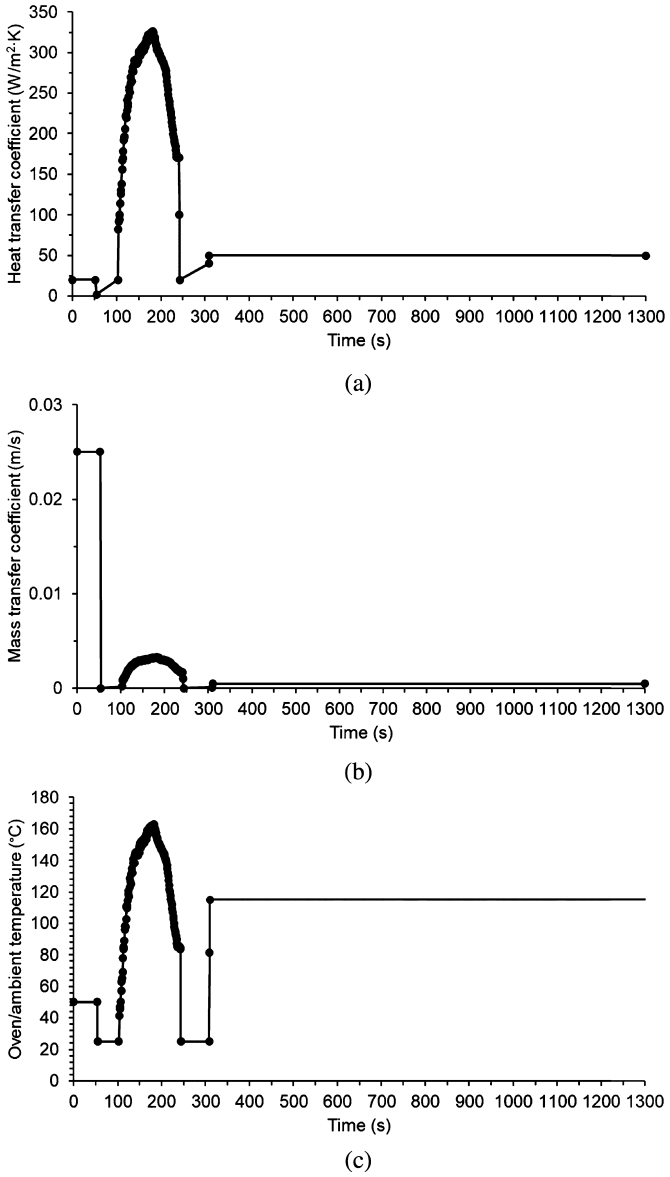

Fig. 7. Simulation inputs (a) heat transfer coefficient (b) mass transfer coefficient (c) oven/ambient temperature.

3. Experimental methodology and model implementation

Sample preparation: The sequential drying experiments were carried out in an industrial facility. The chip was made from individualized quick frozen (IQF) sweet potato, potato, potato flakes, chickpea flour and high oleic sunflower oil (HOSO). The potatoes were peeled, washed with tap water, and diced. A single layer of potato and IQF sweet potato dices was steamed at 100 °C in 100% steam. Approximately 86 g of steamed sweet potato and potato were mashed together and mixed with 11 g of potato flakes, chickpea flour, and 3 g HOSO. The dough was formed into 55 mm diameter and 2 to 3 mm thick discs. The chips passed through a microwave dryer for 1-2 min followed by the impingement dryer for 2 min, and finally through a hot air convection dryer for 10 min as shown in the schematic (Fig. 1).

Shear modulus and glass transition The shear modulus of the chip was measured using the DHT3 Rheometer (TA Instruments, New Castle, DE) with a 5 °C/minute temperature ramp and 25.0 mm parallel plate, Peltier plate Steel 103824 geometry. The initial sample (prepared as mentioned above) of mass 1.01 g ±0.045 g was placed in the rheometer. The temperature of the sample was increased from 35 °C to 155 °C. Uniform heating and hence, the uniform property of the sample, was assumed due to its small size. The shear modulus (± 0.05 MPa) was measured as a function of temperature and showed a transition from a rubbery to a glassy state near 100 °C. During the temperature rise, the sample lost water. As the glass transition temperature is affected by the moisture content, the same experiments were repeated to measure the mass of the sample. The mass of the sample before temperature ramping and at intermediate times (when the temperature reached 55, 65, 75, 85, 95, 105, 115, 125, 135, 145 and 155 °C), was recorded using a balance with an accuracy of 10 μg. All samples, once used for measurement of either moisture or shear modulus, were discarded. The experiments were repeated thrice to increase confidence in the data. From the two sets of data, the shear modulus was obtained as a function of moisture content (Fig. 6).

Water activity measurement: The water activity was measured using a Novasina water activity meter (Novatron Scientific Ltd, Horsham, United Kingdom). A small quantity of the sample was placed in a plastic vessel, which was placed into the water activity meter. The lid was closed, sealing the sample in a small chamber in which the relative humidity was monitored by a humidity sensor. When equilibrium relative humidity was reached at the test temperature of 25 °C (considered to be stable when no change greater than 0.1% in 3 minutes), the reading was displayed. Water activity was calculated by dividing the equilibrium relative humidity (%) by 100. The water activity was measured in replicates of three for the range of moisture content during the sequential drying process.

Temperature, moisture and size validation: The temperature of the chip was measured by inserting a probe near the center using the Scorpion 2 data logger system (Reading Thermal, PA). The probe and the logger instrument were passed through the microwave and the impingement dryer. A separate probe was used to measure the air temperature and velocity in the impingement oven. The temperature at a location near the center was logged every 2 s. The chips were passed through the dryers and samples were taken out every 2 seconds in the microwave dryer, every 30 s in the impingement dryer, and every 5 min in the hot air convection dryer. The weight of the chip was measured immediately after taking it out of the dryer. The chip diameter and thickness were measured using a vernier caliper. A typical dried/partially dried chip (Fig. 9) was reasonably regular shaped in thickness and diameter. The average value of 5 chips was considered to calculate the moisture loss, diameter and thickness.

3.1. Simulation details

The governing equations in the above formulation for the 2D axisymmetric geometry (Fig. 8) were solved in a commercial finite element software (COMSOL Multiphysics 5.6, COMSOL, Burlington, MA) using the PARDISO direct solver in a fully coupled manner. Taking advantage of the symmetry in the sample, 2D-axisymmetric geometry was used. A mapped mesh with 13,726 elements and variable time stepping, with a maximum time step of 1 s and an initial time step of 1 μs, was used following the convergence analysis. The simulation of the sequential drying of 1300 s took approximately 3 h of CPU time on a 3.00 GHz, 24-core each, dual-processor, and 128 GB RAM workstation.

The solid mechanics equations were easier to solve in the Lagrangian frame and, hence, the conservation of linear momentum and the conservation of gas equations were converted to the Lagrangian frame. This was done to simplify the implementation and its coupling with the mechanics physics interface in the software. The conservation of linear momentum (Eq. (17)) was solved in the Lagrangian frame using the Structural Mechanics and the Nonlinear Structural Materials physics interfaces. The hygroscopic swelling sub-module was used to calculate the deformation from the moisture loss. It is important to note that the local concentration, c_w, in Eq. (24) may be higher than the initial concentration due to pressure-driven flow during microwave heating. In such a situation, Eq. (23) will predict swelling instead of shrinkage.

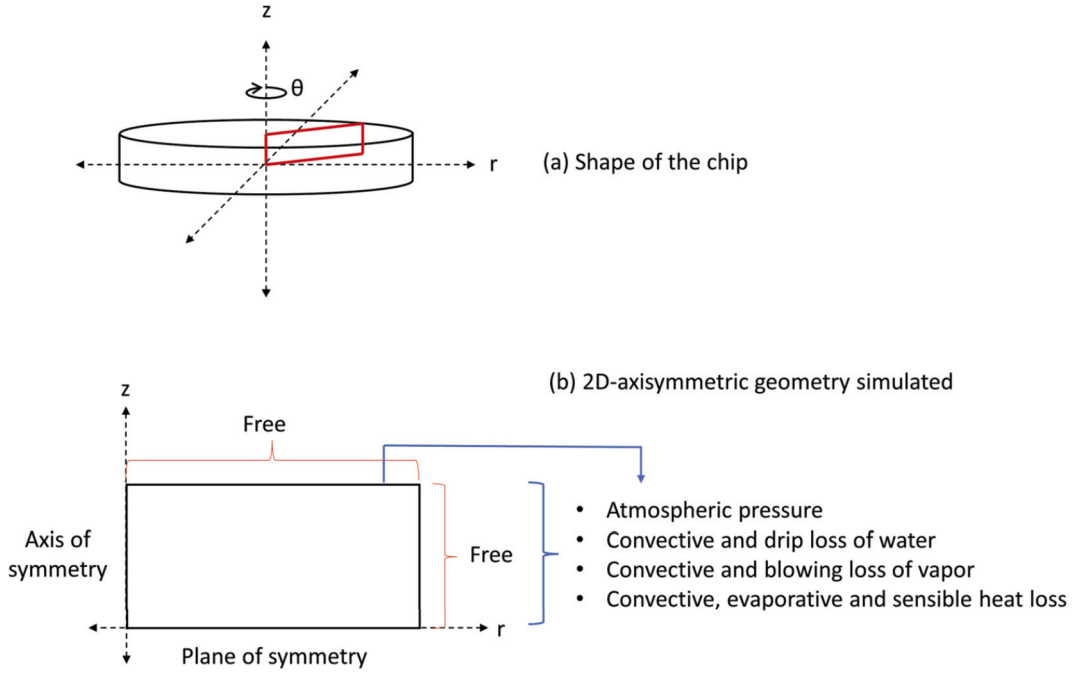

Fig. 8. A schematic showing (a) the actual shape and the 2D axisymmetric computational geometry of the chip and (b) the boundary conditions for transport and solid mechanics for the computational geometry.

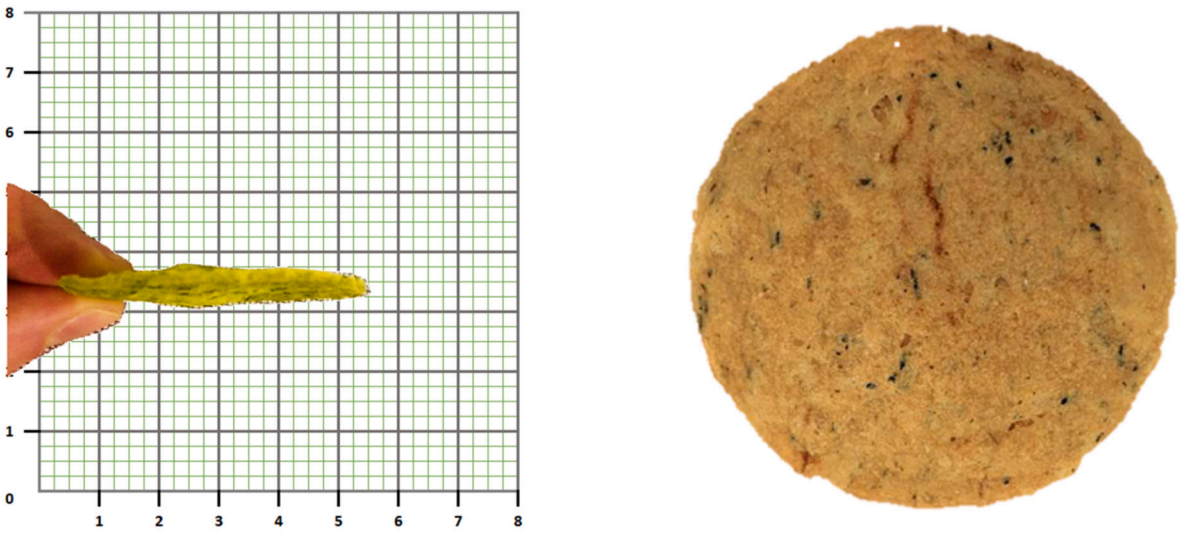

Fig. 9. The thickness (left) and the diameter (right) of the chip were measured using a vernier caliper.

To avoid such a situation, a minimum between the initial concentration, $c_{w,0}$, and the local concentration, c_w, was chosen. Secondly, the concentration also needs to be calculated in the Lagrangian frame. The Lagrangian and Eulerian quantities are equal at t = 0. Considering the porosity in the Lagrangian frame (Coussy, 2004), $\Phi\ (= J\phi)$, and the Lagrangian concentration, c_w^L, can be expressed as $\rho_w \Phi S_w$.

The conservation of water (Eq. (28)) was solved in the Eulerian frame of reference using the Transport of Diluted Species physics interface. The conservation of water vapor (Eq. (29)) and the energy conservation equation were solved in the Eulerian frame of reference using the General form PDE. The conservation of gas (Eq. (30)) was solved using the Darcy's Law physics interface in the Lagrangian frame of reference with appropriate changes as described below. From Eqs. (30), (39) and (42), we can write the gas transport equation in the Eulerian frame,

$$\frac{\partial c_g}{\partial t} + \nabla_x \cdot \underbrace{\left(\rho_g \frac{k_{in,g} f(\phi) k_{r,g}}{\mu_g} \nabla_x p_g \right)}_{\substack{\text{Bulk flow of gas} \\ \text{due to pressure}}} = K_{evp} \phi S_g \left(p_v^{sat} a_w - p_v \right) \frac{M_v}{RT} \tag{64}$$

While writing the above equation in the Lagrangian frame, it should be noted that the function calculating the change in porosity due to deformation, $f(\phi)$, needs to be calculated using the porosity in the Eulerian frame (MacMinn et al., 2016). Although the domain is fixed in the Lagrangian frame, the internal physical structure of the porous medium changes and affects the fluid flow differently. Considering the porosity in the Lagrangian frame (Coussy, 2004), $\Phi = (J\phi)$, the equivalent of Eq. (64) in the Lagrangian frame can be written as

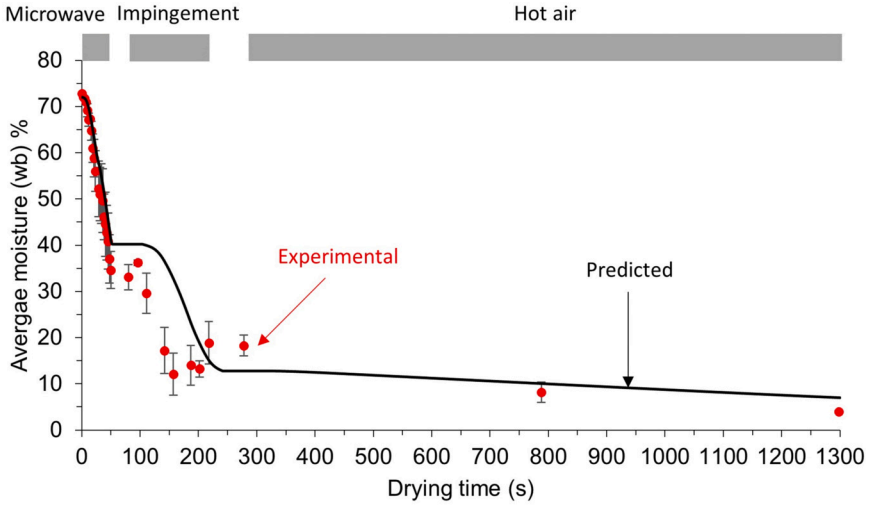

Fig. 10. Predicted and experimentally measured average moisture content (wet basis) in sequential drying.

$$\frac{\partial c_g}{\partial t} + \nabla_X \cdot \left(\underbrace{\rho_g \frac{k_{in,g} f(\phi) k_{r,g}}{\mu_g} \nabla_X p_g}_{\text{Bulk flow of gas due to pressure}} \right) = K_{evp} \Phi S_g \left(p_v^{sat} a_w - p_v \right) \frac{M_v}{RT} \qquad (65)$$

4. Results and discussion

The model was validated against the experimentally measured moisture loss, temperature, diameter and thickness, and total porosity.

4.1. Experimental validation

Moisture histories (Fig. 10) show a good match between the computation and experiment. The moisture loss histories in the microwave dryer and the hot air convection dryer match better than in the impingement dryer (standard deviation 2.7-4.9%). This might be due to more heterogeneous oven conditions and the internal stacking of chips inside the dryer.

The predicted temperature histories near the chip center and close to the chip edge in (Fig. 11a and b) are in good agreement. In the microwave dryer, the temperature rises rapidly. The slight dip in the temperature follows the trend in the microwave power input. Cooler ambient temperature in the microwave dryer results in the chip edge temperature being lower than the center. In the impinger as well as the hot air convection dryer, drying is carried out by the hot air. This results in the temperature near the edge being higher than the center temperature. The predicted temperatures show similar qualitative trends as the ambient air. At the beginning of the impinger, measured temperatures are lower than the predictions due to the time taken during the insertion of thermocouples that were not included in the model. Additionally, the chip deformation during drying may result in thermocouple movement.

The chip diameter predictions match closely with the experiments, while the chip thickness, measured at a non-blistered location, only matches during microwave drying (Fig. 12). Experimental observations show that the chip inflates under microwaves, possibly due to layer separation. Additionally, since the chip was still rubbery at the end of the microwave drying, the puffing that occurred was reverted once the driving force for puffing (microwave heating that generates gas pressure rapidly) was removed. However, during impingement and subsequent hot air drying, the chip transitioned to a glassy state at low moisture content. This resulted in fixing the puffed shape of the chip even after being taken out of the dryer. The physics of blister formation and layer separation is beyond the scope of the current manuscript and needs further study to obtain better validation for the increase in thickness in the impinger.

4.2. Moisture distribution

During microwave drying, the water saturation is higher at the surface (Fig. 13). Since the surface is not completely saturated (i.e., $S_w \approx 1$), the dripping effect is not observed. With water evaporation, the loss of vapor at the boundary also increases. Increased internal evaporation increases the concentration of vapor and, hence, provides higher driving forces for the convective loss of vapor. The convective loss of water at the boundary and the internal evaporation of water primarily remove the moisture from the chip in the microwave dryer and the impinger (Fig. 14). Evaporation of water becomes the dominant mechanism of moisture loss after the initial 25 seconds. This initial period also corresponds to the temperature increases beyond 100 °C (Fig. 11). Water at the surface of the chip evaporates and is lost via convection.

Microwave drying accounts for 50% of the total moisture loss while impingement drying and hot air drying account for 22% and 28% moisture loss, respectively. Out of the total energy input to the chip from the dryers, 66%, 28% and 6% inputs, respectively, are from the microwave, impingement and the hot air dryer.

4.3. Temperature distribution

The temperature of the chip in the microwave dryer does not increase above 100 °C. The microwave energy is used to evaporate water in the chip at initial high moisture conditions (average moisture content is 68%(wb) at 15 s), as opposed to the temperature rise. The volumetric heating and cooler ambient air (50 °C) result in the center of the chip being the hottest during microwave drying (Fig. 15). In the impinger, surface heating and progressive moisture loss result in the chip temperatures increasing much above 100 °C. The hot air dryer maintains an almost uniform temperature (113-114 °C) across the entire chip helping to remove the residual moisture.

4.4. Deformation

Of the total chip shrinkage, 77% was achieved in the microwave dryer, 21.3% in the impingement dryer, and the rest in the hot air dryer. The shrinkage data reflect the moisture loss in each dryer (see Section 4.2) as moisture loss is the primary mechanism of the volume change (Fig. 16a). The other mechanism of volume change, gas pressure gradient, only slightly affects deformation as this driving force is not large enough to expand the material with high bulk modulus. Another

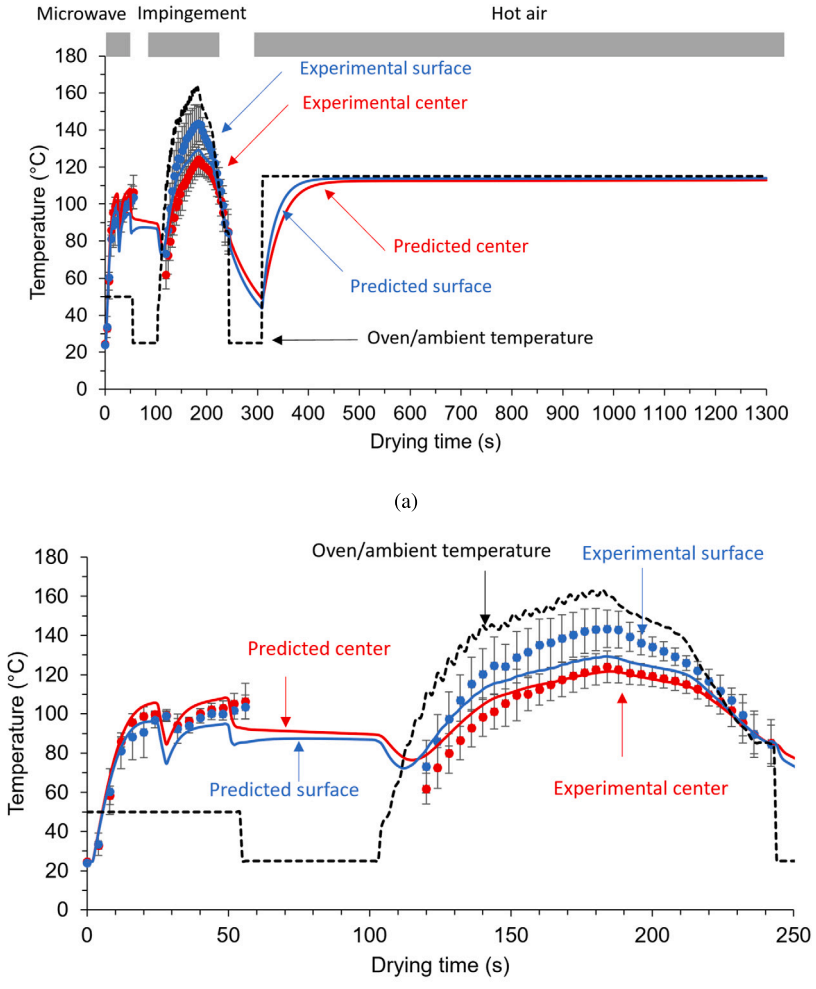

Fig. 11. (a)Predicted and experimentally measured temperatures near the center and at the surface of the chip along with the oven/ambient temperature during sequential drying. (b) Expanded version to show details.

effect of moisture loss being a dominant mechanism is seen through the applicability of the linear elastic constitutive model (Fig. 16b). Although viscous contributions and non-linearity are applicable in theory (Section 2.3.3), the linear viscoelastic and the neo-Hookean constitutive material models show no difference owing to their low contribution to deformation. Thirdly, the shrinkage is expected to be higher at the corner due to higher moisture loss. Although the cross-section of the chip at the center and at the corner appears to be the same (Fig. 14), the thicknesses at these two locations are different (Fig. 16c). The volume change Jacobian also follows the same trend (not shown here).

The chip is initially in the rubbery state characterized by the low shear modulus (Fig. 6b). Since the chip is very thin, it is difficult to characterize the exact location at which the glass transition occurs. Glass transition occurs in the chip into 2/3^{rds} of the impingement drying (185 s) based on the difference between the maximum and minimum value of the shear modulus and the Poisson's ratio (Fig. 17). After the glass transition, the growth in the thickness and the shrinkage in the diameter stops (Fig. 12). As the chip becomes glassy, further shrinkage also decreases as is evident from the small change in the diameter after 185 s (Fig. 12a). In the glassy state, the Poisson's ratio is lower than 0.5 and, hence, the deformation occurs with changes in the elastic volume of the material. Similarly, due to extremely high heat and mass fluxes in the impinger, the material dries faster at the surface than at its core. The dried material acts as an additional resistance to further moisture removal and subsequent shrinkage. Hence, the shrinkage is slowed as the drying progresses in the impingement dryer and the hot air dryer.

4.5. Evaporation rate

The evaporation rate starts to increase from the surface and is the highest at the end of the microwave drying (Fig. 18). The difference between the equilibrium vapor pressure and the partial pressure of vapor drives the evaporation. During microwave drying, internal water rapidly evaporates resulting in the generation of vapor. This increases the internal partial pressure of vapor. Additionally, vapor generated at the surface is carried away by the dry oven air (Halder and Datta, 2012) maintaining a higher driving force for evaporation than at the center. The rate of evaporation reduced after 2/3^{rds} of the impingement was completed. This coincided with the glass transition of the chip. A similar reduction was observed in the case of rice puffing (Gulati and Datta, 2016).

4.6. Pressure generation

Pressure in the impinger decreases for the initial 10 s and starts to increase afterward. The initial reduction is suspected because of the carried-over effect of ambient cooling before the second phase of impingement drying starts. At ambient conditions, the pressure reduces back to atmospheric conditions.

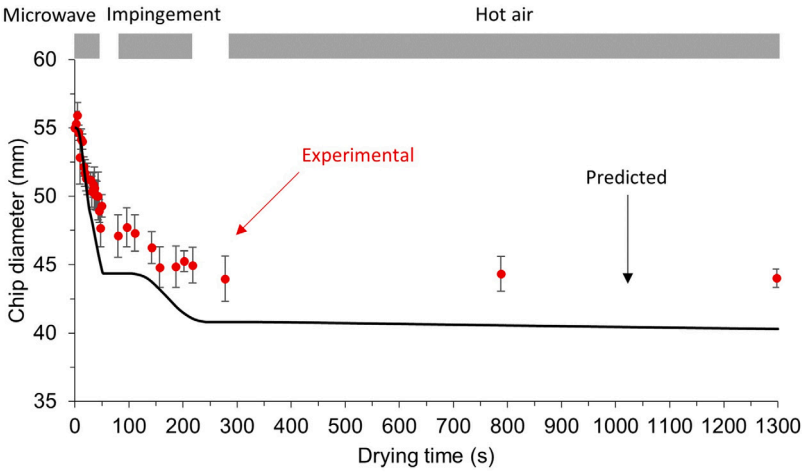

(a)

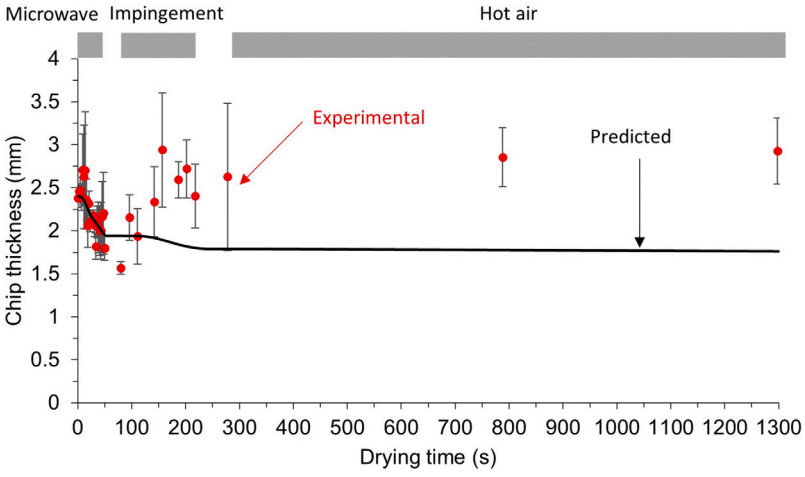

(b)

Fig. 12. Predicted an experimentally measured (a) chip diameter and (b) chip thickness during sequential drying.

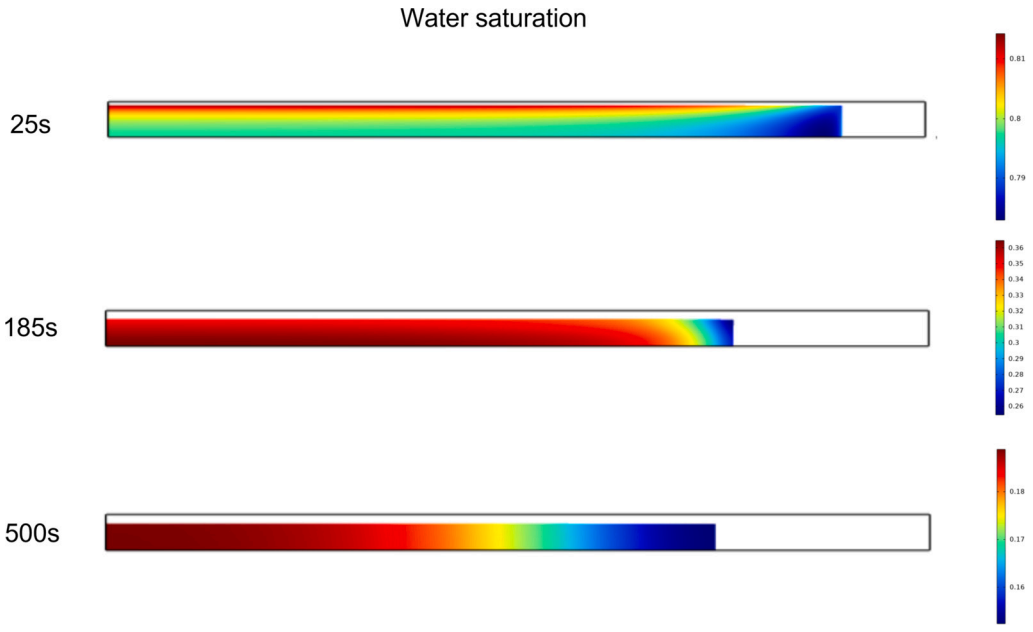

Fig. 13. Spatial distribution of water saturation at various times in the microwave dryer for the axisymmetric computational geometry.

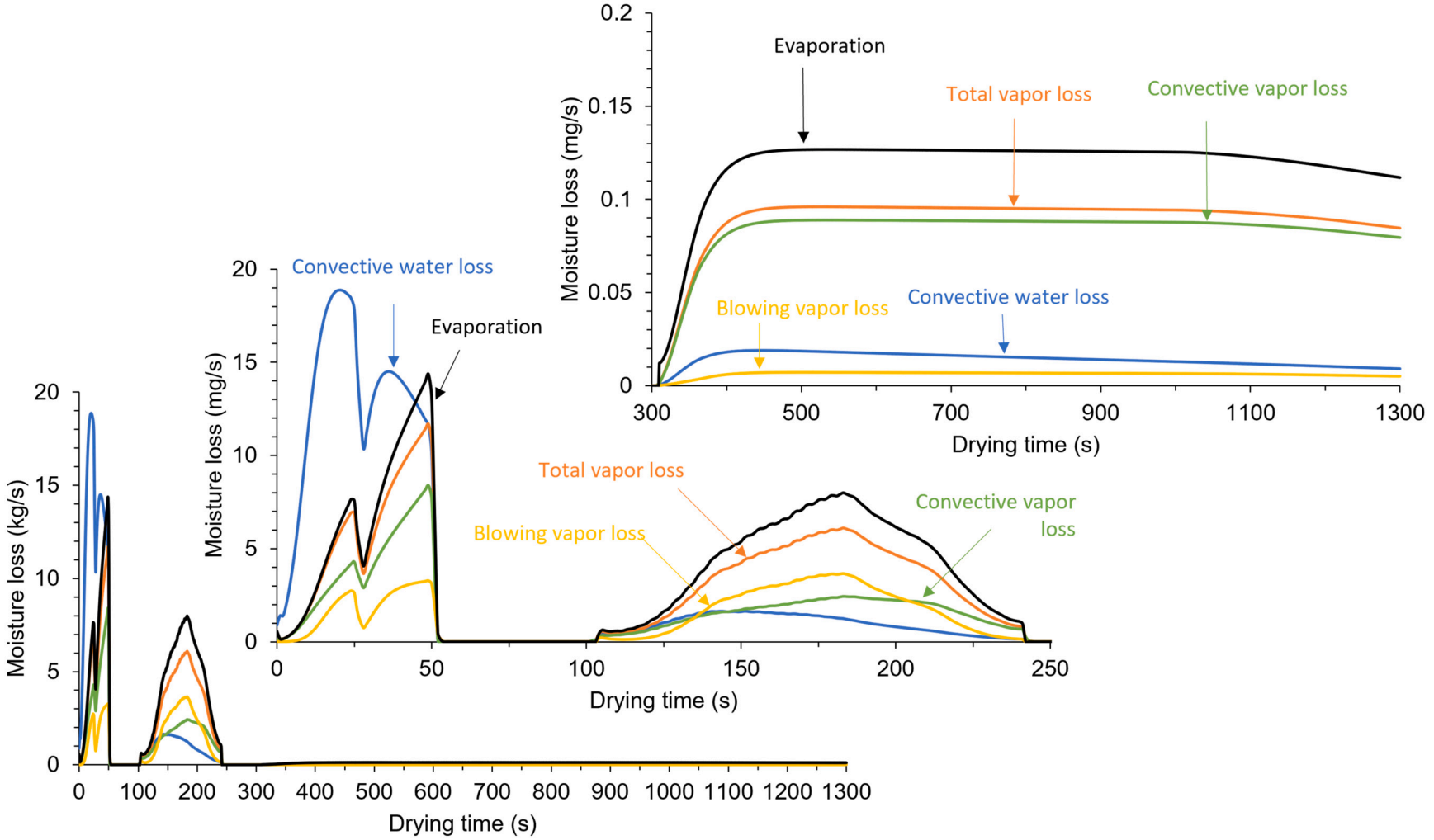

Fig. 14. Mechanism of moisture loss during sequential drying comparing the convective loss of water at the boundary, convective and blowing loss of vapor at the boundary and internal volumetric evaporation. The plot for the microwave and the impingement drying is blown up in the center and the plot for the hot air drying is blown up in the upper right corner.

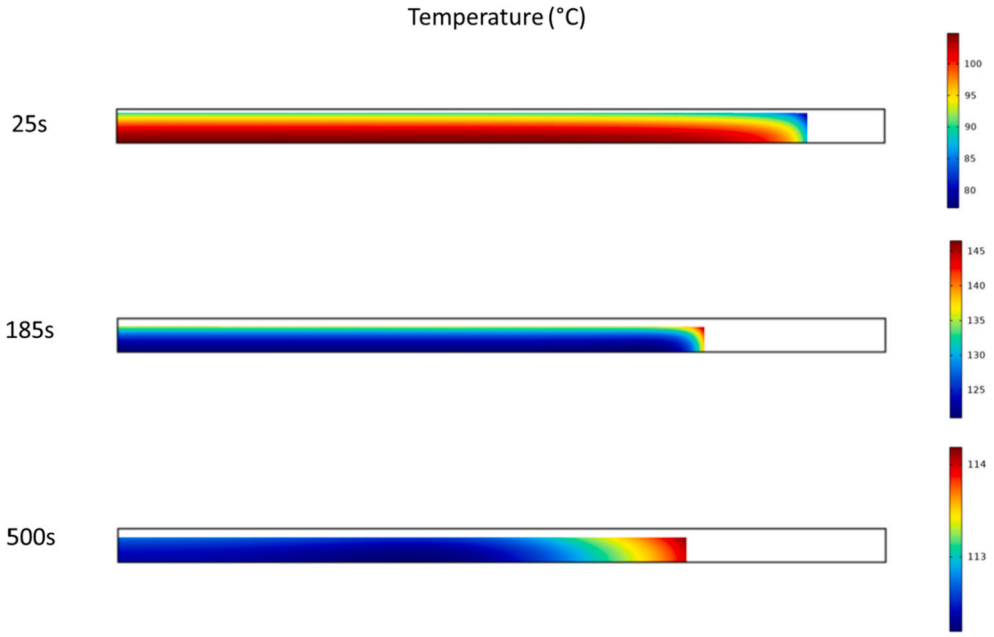

Fig. 15. Spatial distribution of temperature across the chip at different drying times.

The change in pressure also results from the change in the gas permeability of the chip. The internal pressure generated from evaporation acts as a deforming force that expands the chip when it is in the rubbery state. With the expansion, the gas volume fraction in the pore increases. Such changes to the structure of the material facilitate the diffusive and convective transport of vapor (Halder and Datta, 2012; Rakesh and Datta, 2012). This reduces the vapor trapped inside the porous medium and reduces further pressure development. Similarly, the loss of moisture during the drying process removes the water in the pores. For a rubbery material, the lost water represents the loss in volume and, hence, the reduction in porosity. The reduced porosity reduces the permeability through the porosity factor (Eq. (48)). Therefore, the complex effect of change in porosity, gas saturation and evaporation rate alters the pressure in the chip during the sequential drying.

4.7. Comparison with individual drying

To identify and separate the effect of each dryer on the chip texture, with porosity as a surrogate measure, the sequential drying was compared with individual drying processes to achieve the same moisture loss. Four different scenarios were considered here: (S1) sequential drying, (S2) only microwave drying with an average microwave power of combined dryers used as a constant energy input, (S3) only impingement drying with a constant and averaged temperature, and heat and mass transfer coefficients, and (S4) only hot air convection drying. The simulations were continued for different drying times in each scenario (Fig. 19a). S1 removes moisture the fastest (80s) as the energy input from the microwaves is the highest among the four scenarios. All scenarios resulted in the same final volume change (Fig. 19c) and gas porosity (Fig. 19d) as the change in volume is primarily influenced by moisture loss. S3 achieves the desired moisture loss faster (360 s) than S1 (1300 s) but is slow to develop the gas porosity compared to the first two stages of sequential drying. S4 shows the highest drying time (1800 s) because of the slow convective drying.

The main difference among all scenarios was seen in the maximum temperature and internal pressure. Scenario S1 achieved the highest temperatures in its second drying stage (impingement drying). The maximum temperature was predicted at the surface after 75% moisture loss. Scenario S2 predicted the second-highest temperature (Fig. 19b) and the highest pressure. Microwave drying showed higher temperatures at the chip center at low moisture content. The temperature of the chip did not increase much higher than 100 °C until significantly high moisture loss was achieved.

The highest temperature and pressure predictions can be used as quality indicators. At very high temperatures, the flavor and the color of the food can deteriorate due to burning, which leads to reduced quality perception by the consumer; whereas, the highest pressure may affect the quality differently at high and low moisture content.

At high moisture content (scenario S2) the rubbery chip exhibiting lower fracture strength will likely undergo delamination at higher pressure. This may introduce blisters or even explosions at extremely high pressures. At low moisture content (scenario S1), the glassy chip may undergo brittle fractures with large cracks. This may provide the path of least resistance for the generated vapor to escape and will likely reduce the potential expansion. Both cases present additional complexity and are beyond the scope of this manuscript. However, the fundamental understanding of the complex interplay of these phenomena as elucidated in this work can assist product developers in optimizing product quality.

4.8. Sensitivity analysis

A large number of input parameters and material properties are needed to simulate the sequential drying of the chip. An accurate value of all parameters is not always available in the literature. The experimentally measured properties and parameters include variability and uncertainty associated with the measurements and errors. Additionally, varying certain parameters may be of interest for optimization or error margin estimation. Therefore, to have greater confidence in the predicted values, sensitivity analysis is performed for intrinsic permeability, shear modulus and the heat and mass transfer coefficients in the microwave oven.

Permeability: Intrinsic permeability of water and gas in the food greatly affects the drying process. During a drying process, the pore size distribution and the internal structure of the food change. This significantly changes the permeability.

Although part of the change is accounted for through the porosity factor and the relative permeability, the absolute value of permeability reported for a single food material in the literature varies. For a complex food such as a chip that consists of various starches and proteins, sometimes the permeability values are not available in the literature.

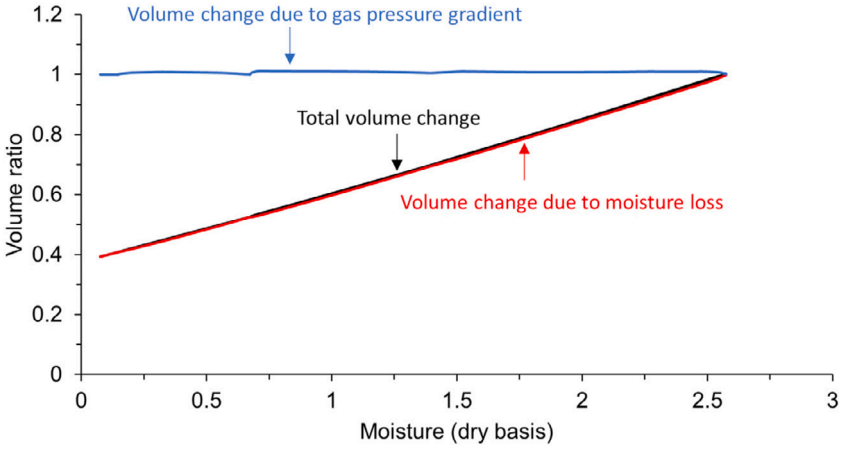

(a)

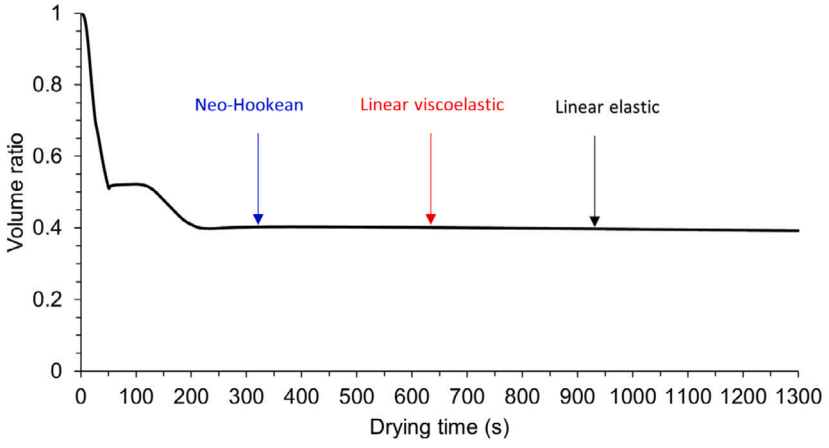

(b)

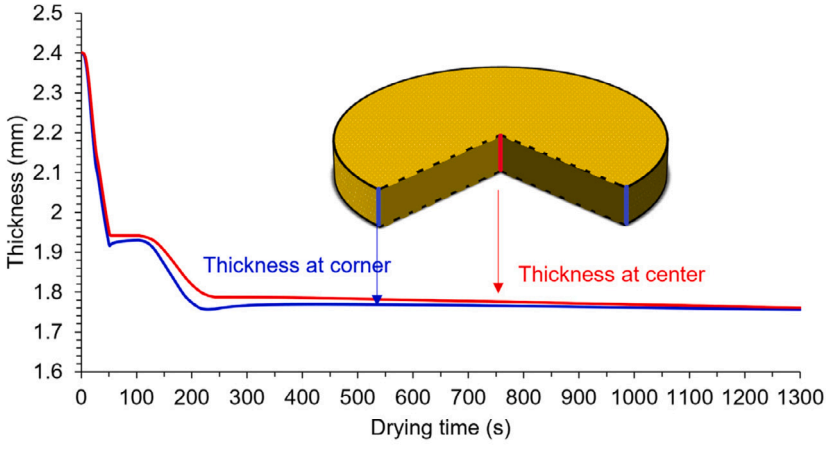

(c)

Fig. 16. (a) Computed changes in total volume due to moisture loss and gas pressure gradient during sequential drying. (b) Computed volume change at the corner of the chip using the linear elastic, linear viscoelastic and neo-Hookean constitutive model. (c) The computed thickness at the center and the at the corner of the chip.

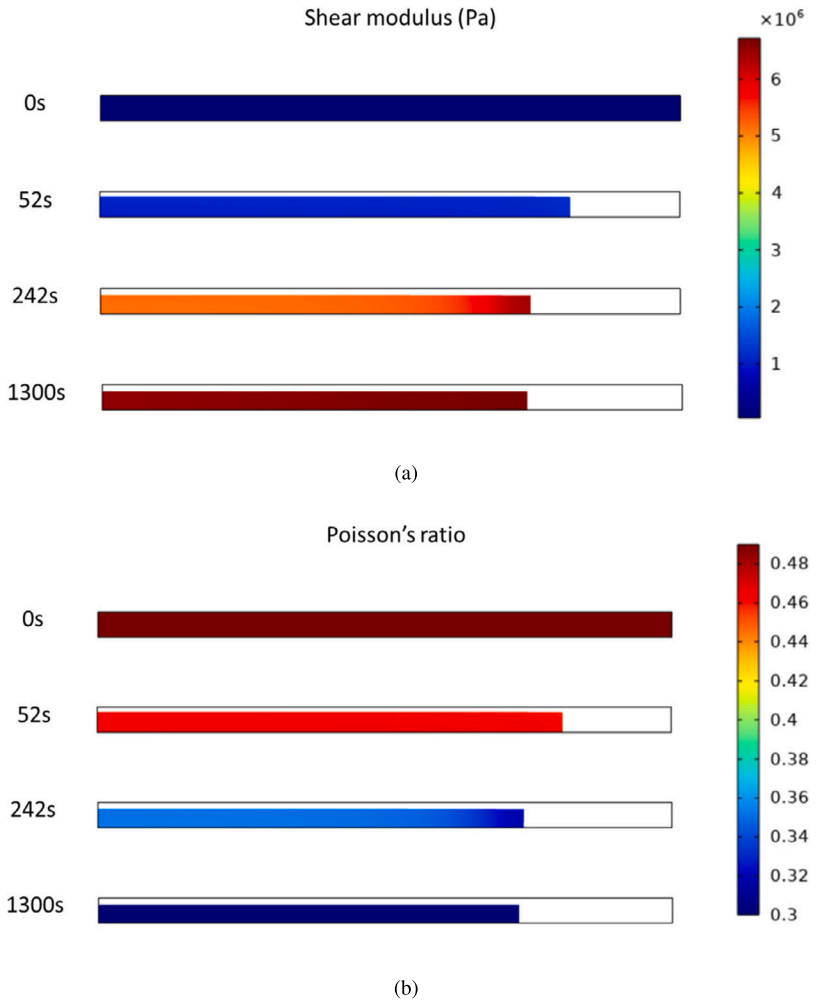

Fig. 17. Spatial distribution of (a) Shear modulus and (b) Poisson's ratio at the beginning (0 s), end of microwave drying (50 s), end of impingement drying (242 s) and the end of the hot air drying.

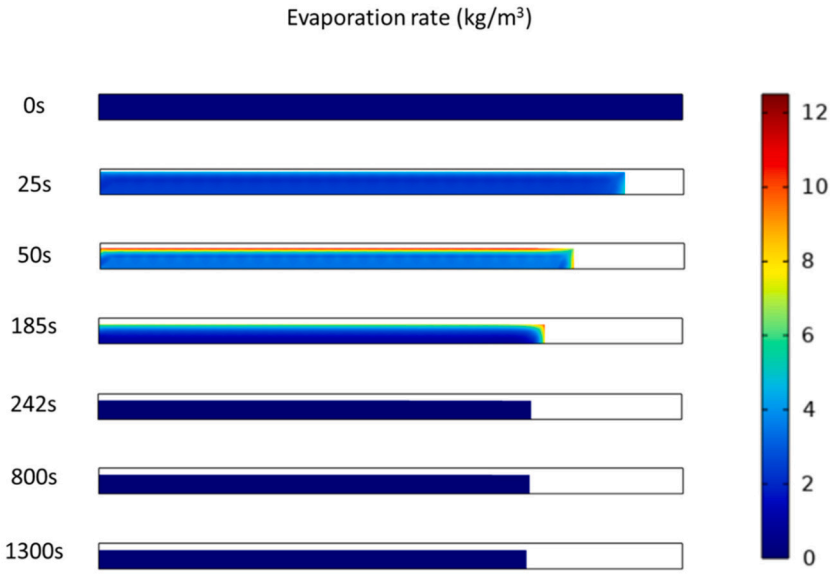

Fig. 18. Evolution in evaporation rate during sequential drying.

Therefore, sensitivity analysis for the permeability was performed by varying the permeability by 1000%, ±50%, ±20%. Average moisture content, the temperature at the center, volume change and the gas porosity were compared to study the effect of permeability. Higher permeability facilitates more moisture loss (Fig. 20a). At higher permeability, the convective flux of water is higher in microwave drying. This

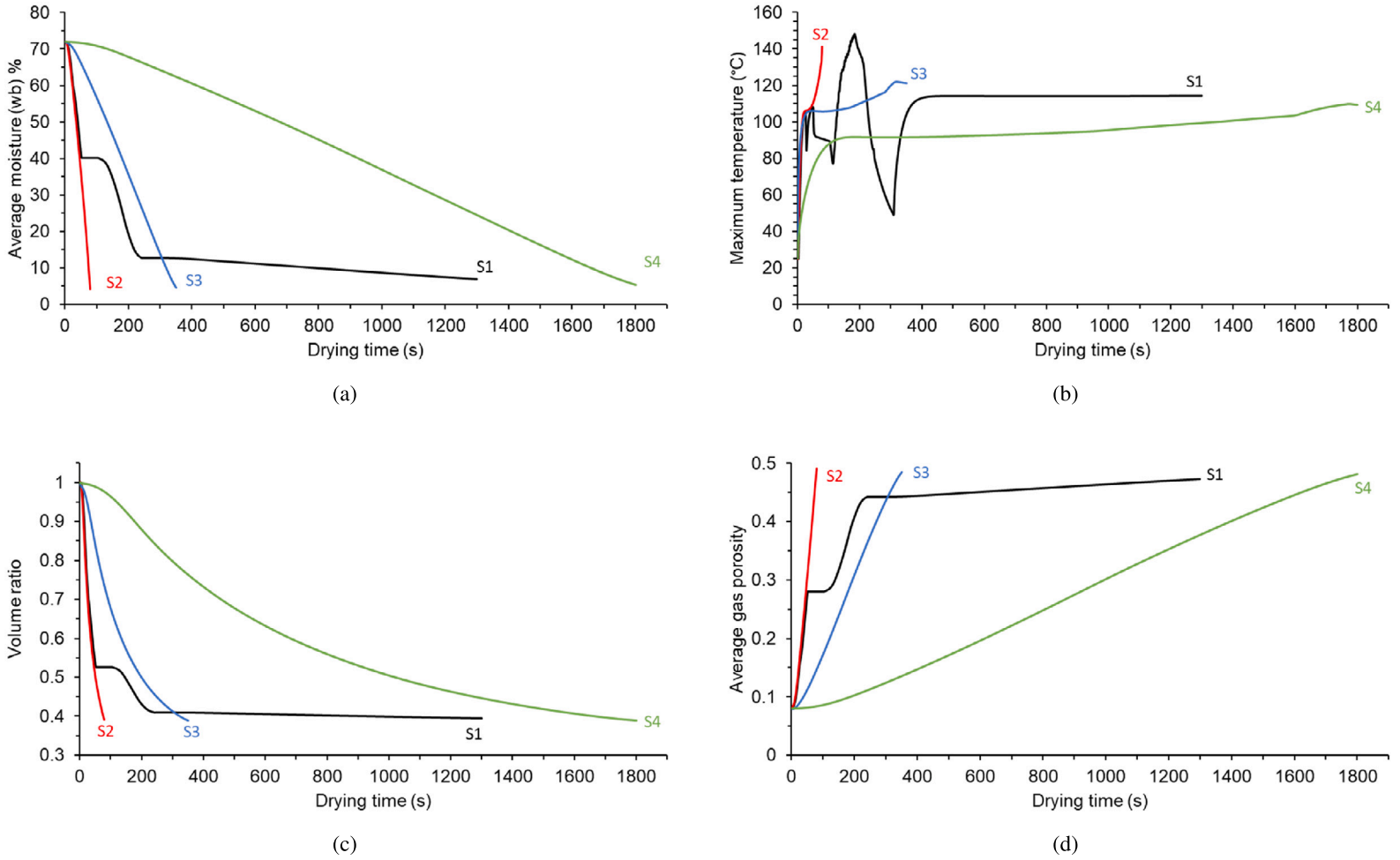

Fig. 19. Computed (a) average moisture content, (b) maximum temperature, (c) ratio of initial to final volume and (d) average gas porosity for combinations of dryers S1 (sequential drying), S2 (only microwave drying), S3 (only impingement drying), S4 (only hot air drying).

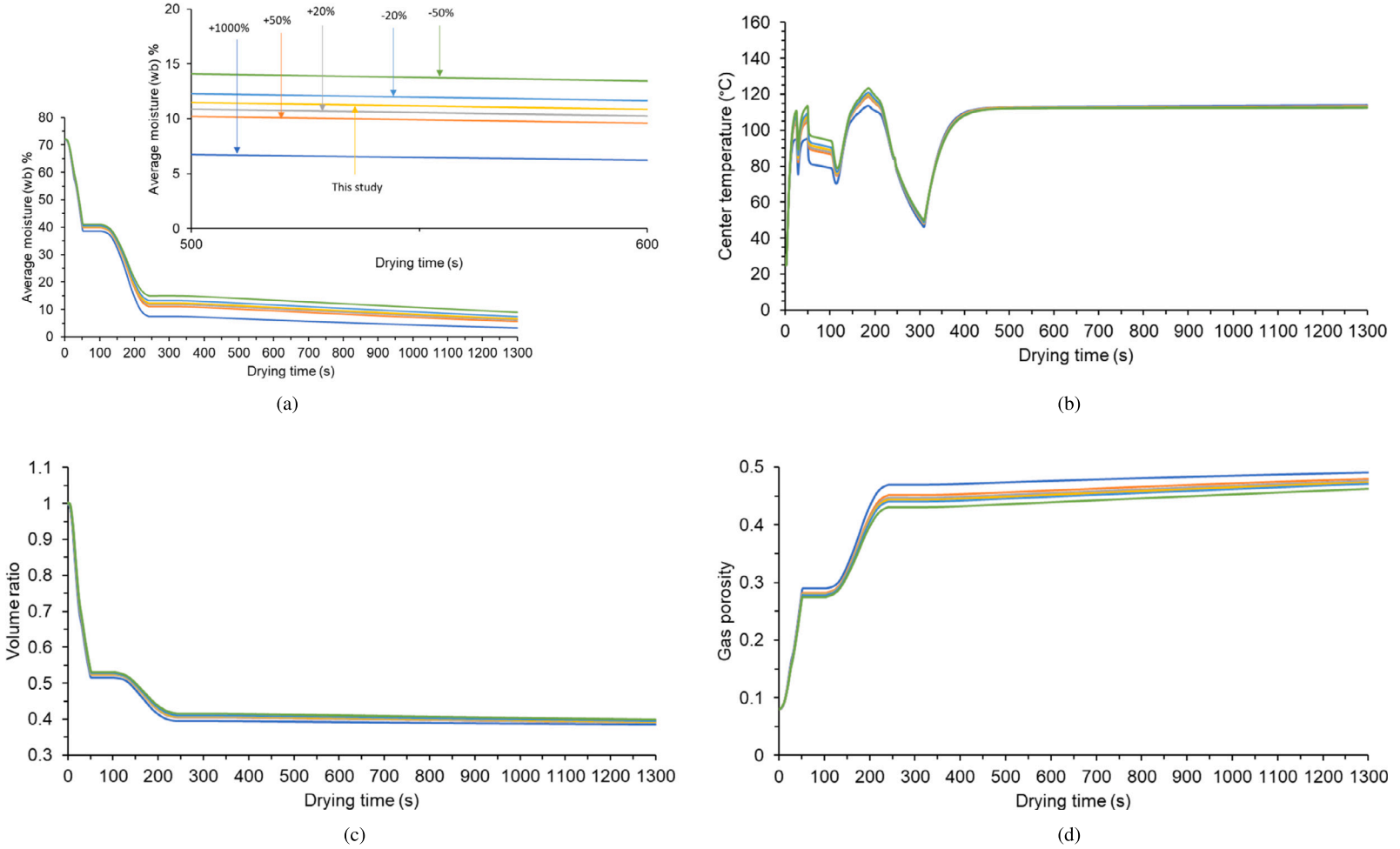

Fig. 20. Computed (a) average moisture content, (b) maximum temperature, (c) ratio of initial to final volume and (d) average gas porosity by varying the permeability by 1000%, ±50%, ±20%.

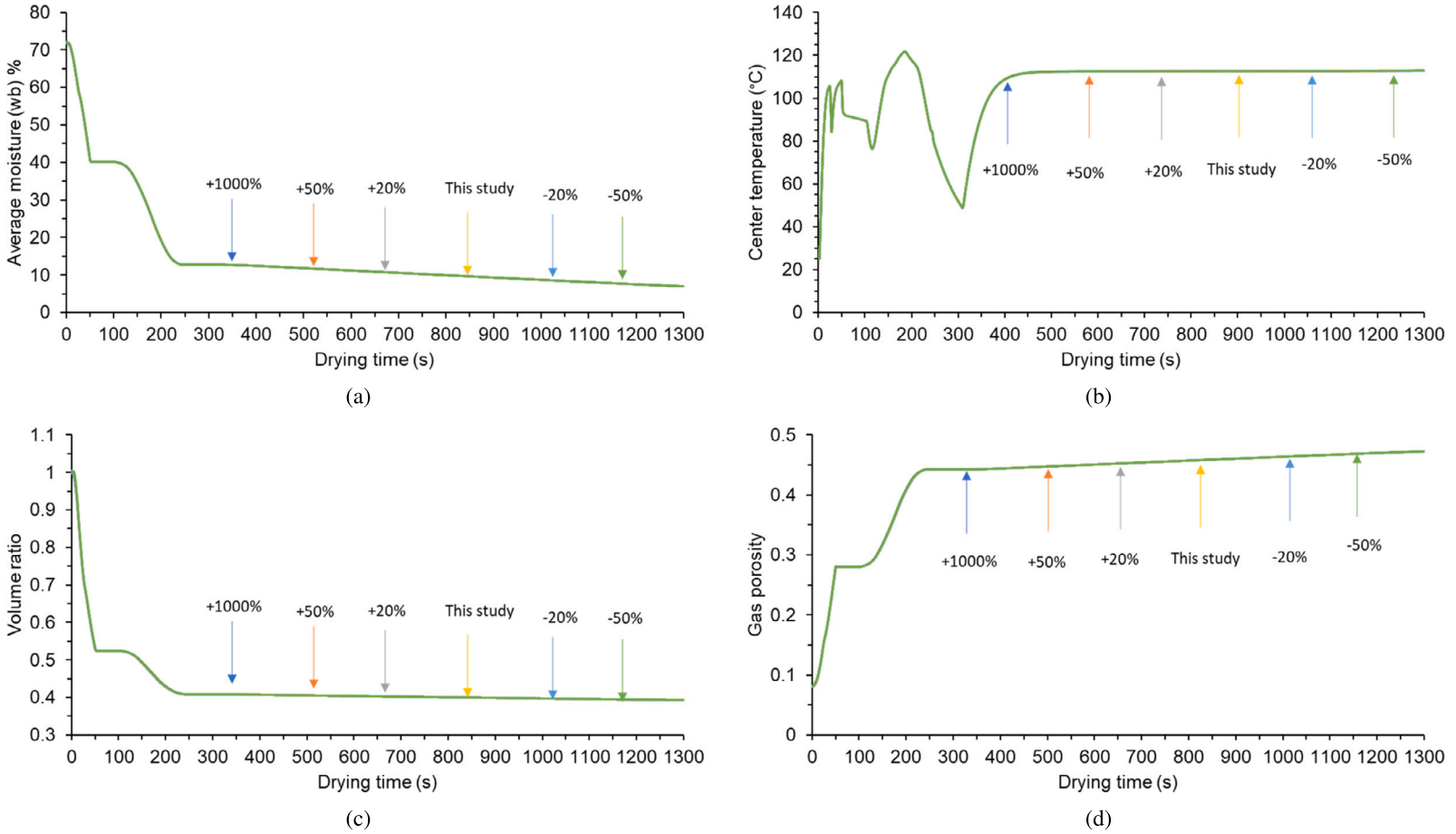

Fig. 21. Computed (a) average moisture content (wb), (b) center temperature, (c) chip diameter and (d) gas porosity of the chip at different drying times when the measured shear modulus values were varied by 1000%, ±50%, ±20%.

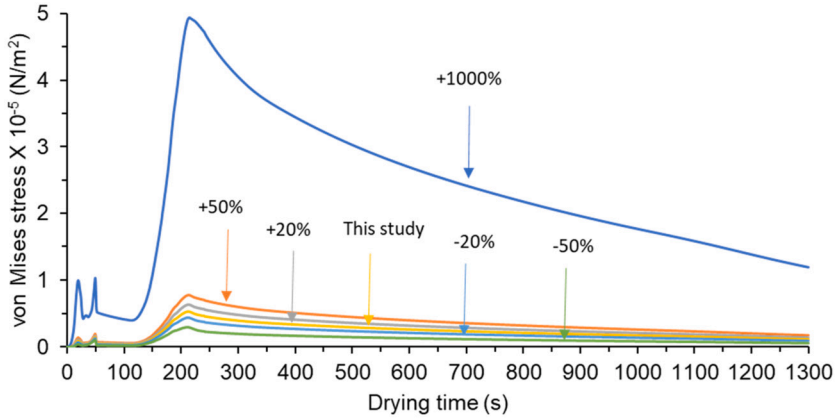

Fig. 22. Computed variation in von Mises stress when the measured shear modulus values were varied by 1000%, ±50%, ±20%.

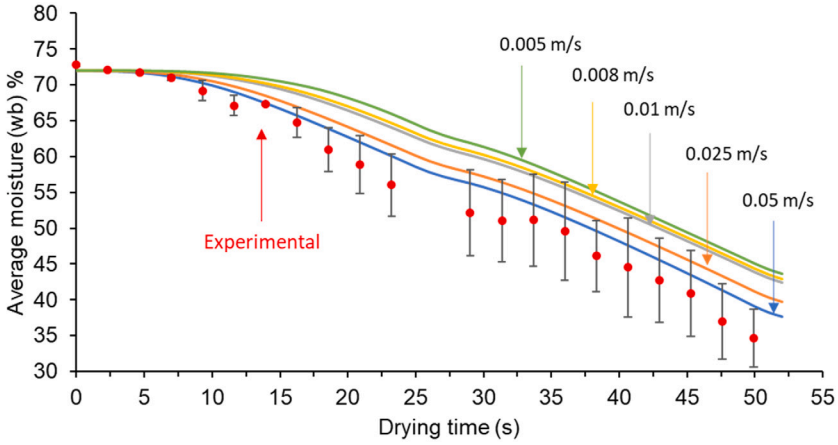

(a)

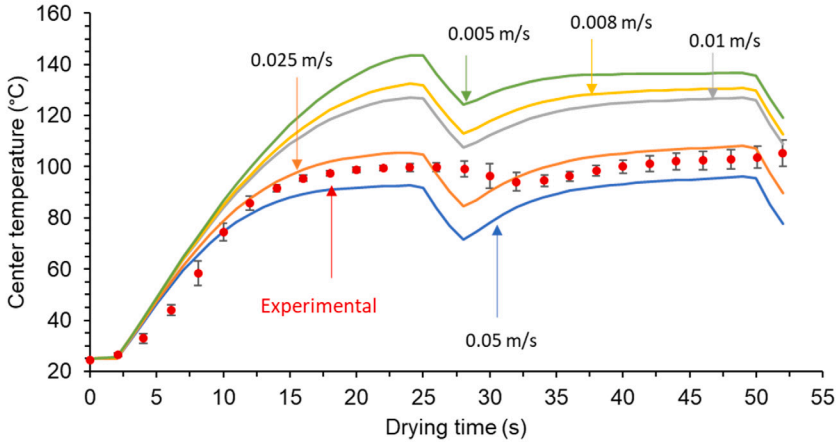

(b)

Fig. 23. Computed variation in (a) average moisture content (wb), (b) center temperature with variation in mass transfer coefficient.

allows more water to be pushed to the surface and results in more water loss. Secondly, as moisture loss is the primary mechanism of deformation, this also results in higher volume change (Fig. 20c) and increased gas porosity (Fig. 20d). As more energy is used towards loss of moisture, this results in lower temperatures (Fig. 20b).

Shear modulus: The shear modulus used in the study was experimentally measured. There is a difference of two orders of magnitude in the values of the shear modulus of raw potato (Yang and Sakai, 2001; Gulati and Datta, 2015) and that of blanched potato (Thussu and Datta, 2012) reported in the literature. The value of shear modulus obtained in this study was in between the range. Although some differences can be attributed to differences in the food material, it is necessary to perform the sensitivity analysis. Hence, the shear modulus was varied by 1000%, ±50%, ±20%. There is hardly any effect of variation in shear modulus

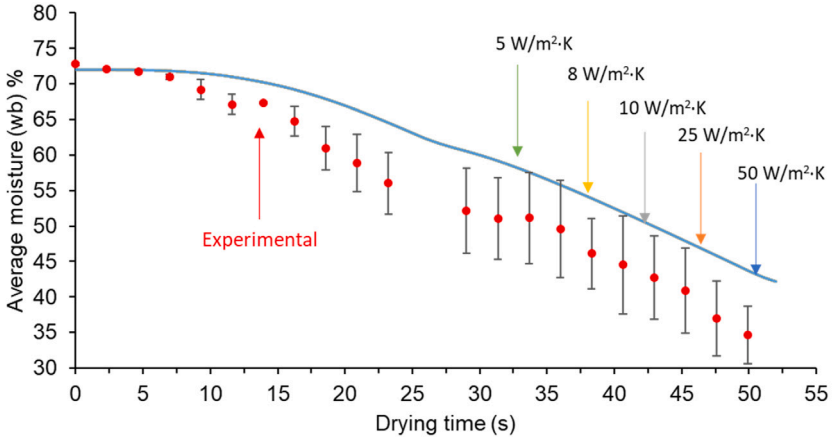

(a)

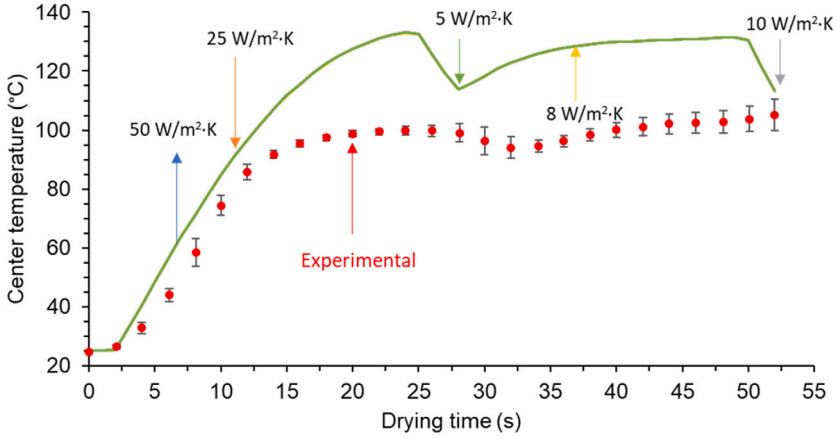

(b)

Fig. 24. Computed variation in (a) average moisture content (wb), (b) center temperature with variation in heat transfer coefficient.

on average moisture content, center temperature, chip diameter and gas porosity (Fig. 21). The transport of water affects the deformation physics (Fig. 3) to a greater extent by changes in the driving forces and the glass transition. However, the effect of deformation in the transport processes is weak as it does not directly affect the driving forces for moisture removal. As other physics are also primarily affected by the moisture concentration (Section 4.2), there is little effect on the chip diameter, center temperature and gas porosity. The effective stress on the food material varied significantly when the shear modulus was varied. An increase in the shear modulus by +1000% showed a nearly 10 times increase in the effective stress (Fig. 22). This has significant implications for the quality during drying. If the effective stress on the solid is higher than the fracture strength of the material then the likelihood of blister formation and delamination will be higher. This can have a significant effect on chip porosity, further drying and the texture of the chip.

It is worth noting that similar characteristic results were predicted for the sensitivity analysis for the elastic modulus of a raw potato during microwave drying (Gulati et al., 2016). Both drying processes are different with regard to material, the intensity of microwave power and sequential drying. As the physics governing drying and deformation of the foods is the same, a similar effect on the quality is expected here as well.

Conditions in microwave drying (heat and mass transfer coefficient): The mass transfer coefficients predicted by the correlations and used in previous studies of microwave drying (Rakesh and Datta, 2012; Ni et al., 1999) varied by one order of magnitude. Therefore, it was necessary to choose the proper value of mass and heat transfer coefficient. Hence, a sensitivity analysis was performed for the mass and heat transfer coefficients during microwave drying. The range of values chosen here represents the difference between the values predicted by the correlation and the values used in this study. Internal evaporation is the primary mechanism of moisture loss in microwave drying (Fig. 13). When the generated vapor can not escape the chip due to resistance at the boundary, the internal concentration of vapor increases. This increases the partial pressure of vapor and decreases further evaporation, the effect of which is seen in two ways: (1) the moisture content of the chip remains high at a low mass transfer coefficient (Fig. 23a) and, (2) the internal chip temperature increases (Fig. 23b) as the energy of microwaves is used for increasing the temperature instead of evaporation of water. This shows that the mechanism of moisture loss at the boundary also affects the internal physics during drying.

In absence of correlations that specifically separate out the effect of convective heat and mass transfer, sensitivity analysis is necessary. Secondly, the heat transfer coefficient does not seem to have a significant effect (Fig. 24a and b) on the transport phenomena in the chip. This possibly is due to the small amount of heat lost at the boundary compared to a large amount of heat used for the internal evaporation of water that affects the transport processes more significantly.

5. Conclusion

A fully coupled model for multi-phase and multi-component transport, large deformation, distributed evaporation, and glass transition was developed, solved and validated for sequential drying of a mashed vegetable chip using microwave, impingement and hot air drying. A comprehensive understanding of quality evolution was obtained by studying the effect of microwave heating, pressure-driven flow, glass transition and change in properties, moisture loss and shrinkage, volumetric evaporation and subsequent pressure generation that reduces the extent of shrinkage and coupling between various physics. The sensitivity of the model to drying conditions in the microwave dryer, gas and water permeability and individual drying methods was also studied. The physics-based framework for the processes and the material transformation being extensive, physical parameters-based quality evolution in various drying processes, drying sequences, and for various materials undergoing significant changes during drying, can be mechanistically understood and optimized following this study. Such practices are a part of computer-aided food engineering that minimizes trial and error, time to market, and resource use (Datta et al., 2022). The model presented in this study, or its data-driven surrogate (Ghosh and Datta, 2023), can be part of a digital twin (Verboven et al., 2020).

The specific conclusions of the study are: (1) The model accurately predicts the moisture loss, temperature, shrinkage, and porosity evolution during sequential drying. (2) Porosity is primarily generated due to moisture loss. (3) The effect of gas pressure is seen through its contribution to reducing the effect of shrinkage. (4) Microwave drying is very intense and affects moisture loss and shrinkage the most. (5) The highest temperature is observed in the impingement dryer. (6) Microwave drying does not increase the temperature much higher than 100 °C as the energy of the microwave is used for water evaporation in the chip at a high moisture content. (7) The hot air convective dryer, with the lowest drying intensity, removes residual moisture and has little effect on the transport of moisture, energy and deformation of the chip. (8) Sequential drying was able to achieve a quality, based on porosity and maximum temperature, that would be hard to achieve using an individual drying method.

Declaration of competing interest

The authors declare the following financial interests/personal relationships which may be considered as potential competing interests: Mayuri Sunil Ukidwe reports financial support was provided by PepsiCo R&D, UK and the grant number 2020-9405536.

Data availability

The authors do not have permission to share data.

Acknowledgement

This research was funded by PepsiCo R&D, UK with the grant number 2020-9405536 as part of a direct contract with Cornell University. The authors' views expressed in the manuscript do not necessarily reflect the position/policy of PepsiCo., Inc. Authors Chris Koh, Stacie Tibos and John Bows are employees of PepsiCo. Inc. Imaging data were acquired through the Cornell Institute of Biotechnology's Imaging Facility, with NIH 1S10OD012287 funding for the Zeiss-Xradia Versa 520 X-ray microscope. This work also made use of the Cornell Center for Materials Research Facilities supported by the National Science Foundation under award Number DMR-1719875.

References

Argyropoulos, D., Heindl, A., Müller, J., 2011. Assessment of convection, hot-air combined with microwave-vacuum and freeze-drying methods for mushrooms with regard to product quality. Int. J. Food Sci. Technol. 46 (2), 333–342.

Bear, J., 1972. Dynamics of Fluids in Porous Media. American Elsevier Publishing Company, New York.

Belytschko, T., Liu, W.K., Moran, B., Elkhodary, K., 2013. Nonlinear Finite Elements for Continua and Structures. John Wiley & Sons.

Bénard, J., Eymard, R., Nicolas, X., Chavant, C., 2005. Boiling in porous media: model and simulations. Transp. Porous Media 60 (1), 1–31.

Benczedi, D., Tomka, I., Escher, F., 1998. Thermodynamics of amorphous starch- water systems. 1. Volume Fluctuations. Macromolecules 31 (9), 3055–3061.

Bird, R.B., Stewart, W.E., Lightfoot, E.N., 2007. Transport Phenomena. revised. J. Wiley & Sons. 12:905.

Chen, J., Pitchai, K., Jones, D., Subbiah, J., 2015. Effect of decoupling electromagnetics from heat transfer analysis on prediction accuracy and computation time in modeling microwave heating of frozen and fresh mashed potato. J. Food Eng. 144, 45–57.

Choi, Y., Okos, M., 1986. Physical and Chemical Properties of Food. American Society of Agricultural Engineers, St. Joseph, Mich.

Cohen, J.S., Yang, T.C., 1995. Progress in food dehydration. Trends Food Sci. Technol. 6 (1), 20–25.

Coussy, O., 2004. Poromechanics. John Wiley & Sons.

Darvishi, H., Khosh, T.M., Najafi, G., Nargesi, F., 2013. Mathematical modeling of green pepper drying in microwave-convective dryer. J. Agric. Sci. Technol. 15, 457–465.

Datta, A., Nicolaï, B., Vitrac, O., Verboven, P., Erdogdu, F., Marra, F., Sarghini, F., Koh, C., 2022. Computer-aided food engineering. Nat. Food, 1–11.

Datta, A.K., van der Sman, R., Gulati, T., Warning, A., 2012. Soft matter approaches as enablers for food macroscale simulation. Faraday Discuss. 158, 435–459.

Dhall, A., Datta, A.K., 2011. Transport in deformable food materials: a poromechanics approach. Chem. Eng. Sci. 66 (24), 6482–6497.

Écsi, L., Ván, P., Fülöp, T., Fekete, B., Élesztős, P., Jančo, R., 2017. A thermoelastoplastic material model for finite-strain cyclic plasticity of metals. arXiv preprint. arXiv:1709.05416.

Eştürk, O., 2010. Drying properties and quality parameters of dill dried with intermittent and continuous microwave-convective air treatments. J. Agric. Sci. 16 (1), 26–36.

Gallego-Castillo, S., Ayala-Aponte, A.A., 2018. Changes in physical properties of sweet potato due to effects of thermal pre-treatments for puree production. Dyna 85 (207), 135–142.

Geedipalli, S., Datta, A., Rakesh, V., 2008. Heat transfer in a combination microwave–jet impingement oven. Food Bioprod. Process. 86 (1), 53–63.

Ghosh, D., Datta, A., 2023. Deep learning enabled surrogate model of complex food processes for rapid prediction. Chem. Eng. Sci. 270, 118515.

Gulati, T., Datta, A.K., 2015. Mechanistic understanding of case-hardening and texture development during drying of food materials. J. Food Eng. 166, 119–138.

Gulati, T., Datta, A.K., 2016. Coupled multiphase transport, large deformation and phase transition during rice puffing. Chem. Eng. Sci. 139, 75–98.

Gulati, T., Zhu, H., Datta, A.K., 2016. Coupled electromagnetics, multiphase transport and large deformation model for microwave drying. Chem. Eng. Sci. 156, 206–228.

Halder, A., Datta, A.K., 2012. Surface heat and mass transfer coefficients for multiphase porous media transport models with rapid evaporation. Food Bioprod. Process. 90 (3), 475–490.

Halder, A., Dhall, A., Datta, A., 2007. An improved, easily implementable, porous media based model for deep-fat frying: Part I: Model development and input parameters. Food Bioprod. Process. 85 (3), 209–219.

Hnin, K.K., Zhang, M., Mujumdar, A.S., Zhu, Y., 2018. Emerging food drying technologies with energy-saving characteristics: a review. Dry. Technol.

Incropera, F.P., DeWitt, D.P., 1990. Fundamentals of Heat and Mass Transfer. John Wiley and Sons, New York.

Khraisheh, M., McMinn, W., Magee, T., 2004. Quality and structural changes in starchy foods during microwave and convective drying. Food Res. Int. 37 (5), 497–503.

Kostaropoulos, A., Saravacos, G., 1995. Microwave pre-treatment for sun-dried raisins. J. Food Sci. 60 (2), 344–347.

Kowalski, S.J., Musielak, G., Banaszak, J., 2010. Heat and mass transfer during microwave-convective drying. AIChE J. 56 (1), 24–35.

Krokida, M., Kiranoudis, C., Maroulis, Z., 1999. Viscoelastic behaviour of dehydrated products during rehydration. J. Food Eng. 40 (4), 269–277.

Krokida, M., Maroulis, Z., 2000. Quality changes during drying of food materials. Drying Technol. Agri. Food Sci. 4 (2), 61–68.

Kumar, C., Karim, M., 2019. Microwave-convective drying of food materials: a critical review. Crit. Rev. Food Sci. Nutr. 59 (3), 379–394.

Kumar, C., Millar, G.J., Karim, M., 2015. Effective diffusivity and evaporative cooling in convective drying of food material. Dry. Technol. 33 (2), 227–237.

MacMinn, C.W., Dufresne, E.R., Wettlaufer, J.S., 2016. Large deformations of a soft porous material. Phys. Rev. Appl. 5 (4), 044020.

Malafronte, L., Lamberti, G., Barba, A.A., Raaholt, B., Holtz, E., Ahrné, L., 2012. Combined convective and microwave assisted drying: experiments and modeling. J. Food Eng. 112 (4), 304–312.

McCabe, W., Smith, J., Harriot, P., 2005. Unit operations of chemical.

McMinn, W., Khraisheh, M., Magee, T., 2003. Modelling the mass transfer during convective, microwave and combined microwave-convective drying of solid slabs and cylinders. Food Res. Int. 36 (9–10), 977–983.

Metaxas, A., Meredith, R.J., 1983. Industrial Microwave Heating. P. Peregrinus on Behalf of the Institution of Electrical Engineers, London, UK.

Moraru, C., Kokini, J., 2003. Nucleation and expansion during extrusion and microwave heating of cereal foods. Compr. Rev. Food Sci. Food Saf. 2 (4), 147–165.

Moreira, R.G., 2001. Impingement drying of foods using hot air and superheated steam. J. Food Eng. 49 (4), 291–295.
Ni, H., 1997. Multiphase Moisture Transport in Porous Media Under Intensive Microwave Heating. Cornell University.
Ni, H., Datta, A., 1999. Heat and moisture transfer in baking of potato slabs. Dry. Technol. 17 (10), 2069–2092.
Ni, H., Datta, A., Torrance, K., 1999. Moisture transport in intensive microwave heating of biomaterials: a multiphase porous media model. Int. J. Heat Mass Transf. 42 (8), 1501–1512.
Nijhuis, H., Torringa, H., Muresan, S., Yuksel, D., Leguijt, C., Kloek, W., 1998. Approaches to improving the quality of dried fruit and vegetables. Trends Food Sci. Technol. 9 (1), 13–20.
Nowak, D., Lewicki, P.P., 2005. Quality of infrared dried apple slices. Dry. Technol. 23 (4), 831–846.
Onwude, D.I., Hashim, N., Abdan, K., Janius, R., Chen, G., 2019. The effectiveness of combined infrared and hot-air drying strategies for sweet potato. J. Food Eng. 241, 75–87.
Özkan-Karabacak, A., Acoğlu, B., Yolci Ömeroğlu, P., Çopur, Ö.U., 2020. Microwave pretreatment for vacuum drying of orange slices: drying characteristics, rehydration capacity and quality properties. J. Food Process Eng. 43 (11), e13511.
Pompe, R., Briesen, H., Datta, A.K., 2020. Understanding puffing in a domestic microwave oven. J. Food Process Eng., e13429.
Qing-Guo, H., Min, Z., Mujumdar, A.S., Wei-hua, D., Jin-cai, S., 2006. Effects of different drying methods on the quality changes of granular edamame. Dry. Technol. 24 (8), 1025–1032.
Rakesh, V., Datta, A.K., 2011. Microwave puffing: determination of optimal conditions using a coupled multiphase porous media–large deformation model. J. Food Eng. 107 (2), 152–163.
Rakesh, V., Datta, A.K., 2012. Transport in deformable hygroscopic porous media during microwave puffing. AIChE J. 59 (1), 33–45.
Rakesh, V., Datta, A.K., Walton, J.H., McCarthy, K.L., McCarthy, M.J., 2012. Microwave combination heating: coupled electromagnetics-multiphase porous media modeling and mri experimentation. AIChE J. 58 (4), 1262–1278.
Ressing, H., Ressing, M., Durance, T., 2007. Modeling the mechanisms of dough puffing during vacuum microwave drying using the finite element method. J. Food Eng. 82 (4), 498–508.
Sanga, E., Mujumdar, A., Raghavan, G., 2002. Simulation of convection-microwave drying for a shrinking material. Chem. Eng. Process. Process. Intensif. 41 (6), 487–499.
Singh, P.P., Maier, D.E., Cushman, J.H., Haghighi, K., Corvalan, C., 2004. Effect of viscoelastic relaxation on moisture transport in foods. Part I: Solution of general transport equation. J. Math. Biol. 49 (1), 1–19.
Souraki, B.A., Mowla, D., 2008. Experimental and theoretical investigation of drying behaviour of garlic in an inert medium fluidized bed assisted by microwave. J. Food Eng. 88 (4), 438–449.
Sperling, L.H., 2005. Introduction to Physical Polymer Science. John Wiley & Sons.
Supmoon, N., Noomhorm, A., 2013. Influence of combined hot air impingement and infrared drying on drying kinetics and physical properties of potato chips. Dry. Technol. 31 (1), 24–31.
Thussu, S., Datta, A.K., 2012. Texture prediction during deep frying: a mechanistic approach. J. Food Eng. 108 (1), 111–121.
Truong, V., Walter Jr., W., Bett, K., 1998. Textural properties and sensory quality of processed sweetpotatoes as affected by low temperature blanching. J. Food Sci. 63 (4), 739–743.
Verboven, P., Defraeye, T., Datta, A.K., Nicolai, B., 2020. Digital twins of food process operations: the next step for food process models? Curr. Opin. Food Sci. 35, 79–87.
Vujošević, L., Lubarda, V., 2002. Finite-strain thermoelasticity based on multiplicative decomposition of deformation gradient. Theor. Appl. Mech. 28 (29), 379–399.
Warning, A., Dhall, A., Mitrea, D., Datta, A.K., 2012. Porous media based model for deep-fat vacuum frying potato chips. J. Food Eng. 110 (3), 428–440.
Witrowa-Rajchert, D., Rząca, M., 2009. Effect of drying method on the microstructure and physical properties of dried apples. Dry. Technol. 27 (7–8), 903–909.
Workneh, T.S., Oke, M.O., 2013. Thin layer modelling of microwave-convective drying of tomato slices. Int. J. Food Eng. 9 (1), 75–90.
Yang, B., Huang, W.M., Li, C., Chor, J.H., 2005. Effects of moisture on the glass transition temperature of polyurethane shape memory polymer filled with nano-carbon powder. Eur. Polym. J. 41 (5), 1123–1128.
Yang, H., Gunasekaran, S., 2001. Temperature profiles in a cylindrical model food during pulsed microwave heating. J. Food Sci. 66 (7), 998–1004.
Yang, H., Sakai, N., 2001. Shrinkage and mechanical characteristics of potato undergoing air convection drying. Jpn. J. Food Eng. 2 (2), 67–71.
Yin, X., Jiao, S., Sun, Z., Qiu, G., Tu, K., Peng, J., Pan, L., 2019. Two-step drying based on air jet impingement and microwave vacuum for apple slices. J. Food Process Eng. 42 (5), e13142.
Young, R.J., Lovell, P.A., 2011. Introduction to Polymers. CRC Press.
Zhang, H., Datta, A., 2003. Microwave power absorption in single- and multiple-item foods. Food Bioprod. Process. 81 (3), 257–265.
Zhang, M., Chen, H., Mujumdar, A.S., Tang, J., Miao, S., Wang, Y., 2017. Recent developments in high-quality drying of vegetables, fruits, and aquatic products. Crit. Rev. Food Sci. Nutr. 57 (6), 1239–1255.
Zhao, D., An, K., Ding, S., Liu, L., Xu, Z., Wang, Z., 2014. Two-stage intermittent microwave coupled with hot-air drying of carrot slices: drying kinetics and physical quality. Food Bioprocess Technol. 7 (8), 2308–2318.
Zhou, X., Wang, S., 2019. Recent developments in radio frequency drying of food and agricultural products: a review. Dry. Technol. 37 (3), 271–286.